# Stress conditions and seismic activity around the rupture zone of the 2016 Kumamoto earthquake in Kyushu, southwest Japan

Michiharu Ikeda[1], Kozo Onishi[2], and Naoki Nishizaka[3]

[1]Shikoku Research Institute Incorporated
[2]Shikoku Electric Power Co. Inc.
[3]Shikoku Electric Power Company Incorporated

November 24, 2022



### Abstract

The main events of the 2016 Kumamoto earthquake in Kyushu were a foreshock (Mw 6.2) on 14 April and the main shock (Mw 7.0) on 16 April 2016, both of which were caused by fault ruptures near the intersection of the Futagawa and Hinagu fault zones. However, not all sections of the two fault zones were ruptured during the earthquake. In particular, the northernmost (Takano-Shirahata) section of the Hinagu fault zone ruptured, but the rupture did not propagate to southern sections of the fault zone. We examined fault geometry and paleoseismological data of the fault zones, and furthermore used numerical analyses to investigate rupture conditions around the source faults of the earthquake, which together allowed us to consider the potential for future earthquakes in the region. Fault geometry, slip tendencies, and fault rupture history indicated that the rupture potential on the source faults was high before the earthquake. Seismicity and rupture propagation during the earthquake sequence were probably controlled by geological heterogeneities of the fault zones. Coulomb stress change analysis indicated that stress transfer from the source faults to the Hinagu section during the earthquakes was smooth, and that most of that section received a positive stress change. This stress change and the high slip tendencies we calculated for the Hinagu section indicate that it has high potential for a future rupture. These results provide crucial information for preparation for disaster mitigation of future earthquakes around the rupture zone of the 2016 Kumamoto earthquake.

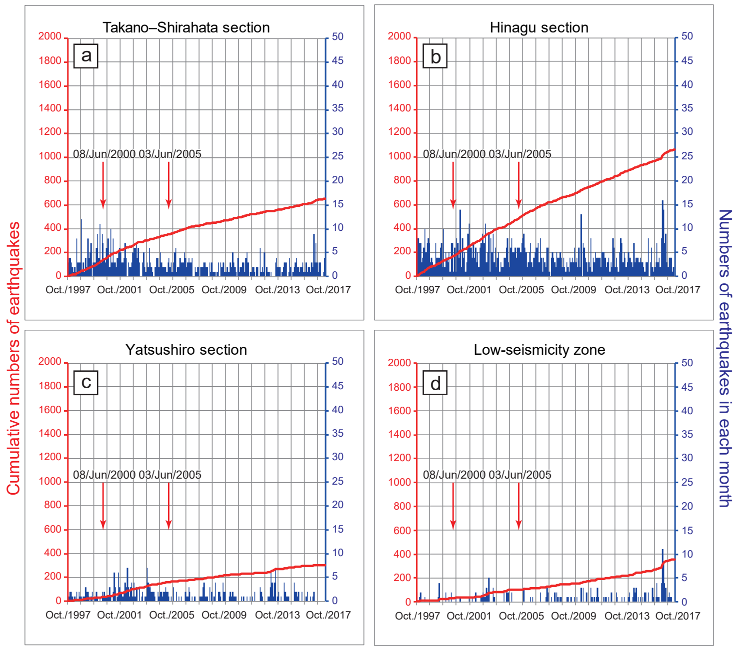

Takano–Shirahata section
Hinagu section
Yatsushiro section
Low-seismicity zone
a
b
c
d
08/Jun/2000
03/Jun/2005
Oct./1997
Oct./2001
Oct./2005
Oct./2009
Oct./2013
Oct./2017
Cumulative numbers of earthquakes
Numbers of earthquakes in each month

# Stress conditions and seismic activity around the rupture zone of the 2016 Kumamoto earthquake in Kyushu, southwest Japan

Michiharu Ikeda[1*], Kozo Onishi[2], and Naoki Nishizaka[2]

[1]Department of Civil Engineering, Shikoku Research Institute Inc., 2109-8 Yashimanishimachi, Takamatsu 761-0192, Japan

[2]Department of Civil and Architectural Engineering, Shikoku Electric Power Company Inc., 2-5 Marunouchi, Takamatsu 760-8573, Japan

* Corresponding author. Tel: +81-50-8802-4788

E-mail: m-ikeda@ssken.co.jp

## Key points

Rupture conditions before the 2016 Kumamoto earthquake indicated that rupture of the Takano–Shirahata section was likely.

Southward rupture propagation of the 2016 Kumamoto earthquake was curtailed by the geological heterogeneity in the Hinagu section.

The potential for delayed earthquakes following the 2016 Kumamoto earthquake in the Hinagu fault zone is high.

## Abstract

The main events of the 2016 Kumamoto earthquake in Kyushu were a foreshock ($M_w$ 6.2) on 14 April and the main shock ($M_w$ 7.0) on 16 April 2016, both of which were caused by fault ruptures near the intersection of the Futagawa and Hinagu fault zones. However, not all sections of the two fault zones were ruptured during the earthquake. In particular, the northernmost (Takano–Shirahata) section of the Hinagu fault zone ruptured, but the rupture did not propagate to southern sections of the fault zone. We examined fault geometry and paleoseismological data of the fault zones, and furthermore used numerical analyses to investigate rupture conditions around the source faults of the earthquake, which together allowed us to consider the potential for future earthquakes in the region. Fault geometry, slip tendencies, and fault rupture history indicated that the rupture potential on the source faults was high before the earthquake. Seismicity before the earthquake and rupture propagation during the earthquake sequence were probably controlled by geological heterogeneities of the fault zones. Coulomb stress change analysis indicated that stress transfer from the source faults to the Hinagu section during the earthquakes was smooth, and that most of that section received a positive stress change. This stress change and the high slip tendencies we calculated for the Hinagu section indicate that it has high potential for a future rupture. These results provide crucial information for preparation for disaster mitigation of future earthquakes around the rupture zone of the 2016 Kumamoto earthquake.

Key words: 2016 Kumamoto earthquake, Futagawa fault zone, Hinagu fault zone, slip tendency, low-seismicity zone, Coulomb stress change

## 1. Introduction

The 2016 Kumamoto earthquake included a foreshock ($M_w$ 6.2) on 14 April 2016, which was followed by the main shock ($M_w$ 7.0) on 16 April, with an epicenter close to that of the foreshock (Figure 1). Both the foreshock and aseismic slip probably loaded stress onto the faults that ruptured during the main shock (Kato et al., 2016). The results of detailed geological, geodetic, and seismological studies conducted since the 2016 Kumamoto earthquake indicate that the fault ruptures occurred in the Futagawa fault zone (including a previously unknown 5 km extension to the northeast) and the northern part of the Hinagu fault zone (Asano & Iwata, 2016; Fukahata & Hashimoto, 2016; Geospatial Information Authority of Japan, 2016; Kobayashi, 2017; Shirahama et al., 2016; Sugito et al., 2016; Toda et al., 2016). The Futagawa and Hinagu fault zones have been recognized as active fault zones on the basis of paleoseismological data (Headquarters for Earthquake Research Promotion (HERP), 2013). HERP (2013) has indicated that the probability of future seismic activity in both of these fault zones is high.

Fault ruptures are often initiated or arrested in areas around discontinuities in the trends of the faults or fault zones, such as fault bends or intersections (Biasi & Wesnousky, 2016; King, 1986; King & Nabelek, 1985; Wesnousky, 2006). Consistent with these study findings, the epicenters of the foreshock and main shock of the 2016 Kumamoto earthquake are both near the intersection of the Futagawa and Hinagu fault zones (Figure 1). However, not all sections of the two fault zones were ruptured during the earthquake. In particular, the northernmost section (Takano–Shirahata section) of the Hinagu fault zone ruptured, but southwestward propagation of the rupture within the Hinagu fault zone was arrested, despite the lack of a fault discontinuity such as a large bend or step structure (e.g., Uchide et al., 2016).

Three intriguing questions about the 2016 Kumamoto earthquake remain to be answered: Why did the Futagawa and Hinagu fault zones rupture? Why was the rupture of the Hinagu fault zone arrested at the southern end of the Takano–Shirahata section? What is the seismic potential of the Hinagu section since the 2016 Kumamoto earthquake? To answer these questions, we first used the slip tendency analysis method of Morris et al. (1996) to investigate the seismic potential of the Futagawa and Hinagu fault zones under the regional stress field that preceded the 2016 Kumamoto earthquake. We then analyzed background seismicity before the 2016 Kumamoto earthquake sequence to understand seismic conditions around the fault zones at that time. Finally, we calculated the stress perturbation caused by the 2016 Kumamoto earthquake to evaluate static stress transfer. The results of these analyses, together with local geological structures and paleoseismological data, allowed us to infer rupture conditions around the source faults of the 2016 Kumamoto earthquake and the possibility of future earthquakes in the area.

## 2. Slip Tendency Analysis to Evaluate Seismic Potential along the Futagawa and Hinagu Fault Zones

### 2.1. Slip Tendency Analysis Method

Slip potential of a fault depends on regional stress conditions, fault geometry, and the coefficient of friction $\mu$ in the fault plane. Morris et al. (1996) proposed that slip tendency analysis can be a valuable tool for evaluating the inherent slip potential of a fault. They defined the slip tendency (*Ts*) on a fault surface as the ratio of the shear stress ($\tau$) to the normal stress ($\sigma_n$) on that fault.

$$Ts = \tau/\sigma_n \quad (1)$$

Thus, *Ts* is equal to the coefficient of sliding friction. The likelihood of a slip is high when the slip tendency is high, and it is low when the slip tendency is low. The slip tendency is computed by assuming that the envelope of Coulomb frictional sliding, which is dependent on the friction coefficient on the fault plane, is tangential to the Mohr circle (Lisle & Srivastava, 2004). Therefore, $Ts' = Ts/\max(Ts) = Ts/\mu'$; here, $\mu'$ is the apparent friction coefficient (explained below), and $Ts'$ ranges from 1 for a fault with a near-ideal orientation for slip, to 0 when the fault plane is perpendicular to the maximum principal stress direction. In this study, we analyzed the slip tendency, represented by $Ts'$, using the slip tendency analysis software developed by Neves et al. (2009).

To calculate the slip tendency, the following are required: (1) a fault plane model, (2) the directions of the principal stress axes, and (3) the stress ratio ($R = (\sigma_2 - \sigma_1) / (\sigma_3 - \sigma_1)$). In this study, we set $\mu'$ to 0.4 because friction coefficients of 0.15–0.55 (i.e., much lower than the value of 0.6 reported by Byerlee (1978) for intact rocks) have been reported for a clay-rich fault gouge along the San Andreas Fault (Bos & Spiers, 2002; Morrow et al., 1992; Niemeijer & Spiers, 2005). Therefore, $\mu'$ is the apparent friction coefficient taking into consideration the effects of fault damage and pore pressure. We set the Poisson ratio to 0.25, because an average ratio of *Vp*/*Vs* of rocks in crust is estimated to be 1.73.

To calculate the slip tendency, we created a fault plane model (Table S1) based on HERP (2013) and Asano & Iwata (2016). HERP (2013) divided the Futagawa and Hinagu fault zones into three sections each as follows. The Futagawa fault zone comprises the Futagawa, Uto, and Northern Coast of Uto Peninsula (NCUP) sections, and the Hinagu fault zone comprises the Takano–Shirahata, Hinagu, and Yatsushiro sections (HERP, 2013) (Figure 1). The fault models for the Takano–Shirahata and Futagawa sections that we used in our analysis are derived from the waveform inversion analysis results reported by Asano and Iwata (2016) (Table S1). The locations of the other fault sections are as in HERP (2013). However, HERP (2013) do not provide detailed information about dip angles of the fault planes in the Futagawa and Hinagu fault zones. The dip angle of the Hinagu section is estimated to be 70° from the aftershock distribution of the 2016 Kumamoto earthquake, following Yano and Matsubara (2017). Additionally, the dip angle of the Yatsushiro section is inferred to be roughly vertical, based on the hypocenter distribution of background seismicity (Figure S1). The dip angles of the Uto and NCUP sections of the Futagawa fault zone have not been estimated, because there is less seismicity along these fault sections. Therefore, we calculated slip tendencies of these fault sections for three dip angle cases (40°, 70°, and 90°).

Matsumoto et al. (2015) estimated the two-dimensional stress field on Kyushu Island by using the stress-tensor inversion method and reported a mixed stress regime of both strike-slip and normal faulting for the source faults of the 2016 Kumamoto earthquake. However, it is well accepted that strike-slip faulting was dominant during the earthquake (Asano & Iwata, 2016; Fukahata & Hashimoto, 2016; Geospatial Information Authority of Japan, 2016; Kobayashi, 2017; Shirahama et al., 2016; Sugito et al., 2016; Toda et al., 2016). We therefore assumed that a strike-slip faulting stress regime was dominant around the source faults of the 2016 Kumamoto earthquake. We could not uniquely determine the direction of the maximum principal stress ($\sigma_1$) in the horizontal plane around the Futagawa and Hinagu fault zones. Therefore, in the slip tendency calculations, we considered three possible orientations of $\sigma_1$, N55°E, N70°E, and N85°E, around the Futagawa and Hinagu fault zones based on the principal directions of the stress tensor reported by Matsumoto et al. (2015).

In their examination of the local tectonic stress field, Matsumoto et al. (2015) used the stress ratio $\phi = (\sigma_2 - \sigma_3) / (\sigma_1 - \sigma_3)$, which corresponds to $(1 - R)$. They then determined the spatial distribution of stress ratios on Kyushu Island. For the strike-slip faulting stress regime around the Futagawa and Hinagu fault zones (see figure 3a of Matsumoto et al., 2015), they estimated $\phi' = (\sigma_H - \sigma_h) / (\sigma_v - \sigma_h)$ to be 1.0–2.0, where $\sigma_H$ and $\sigma_h$ are the maximum and minimum principal stresses in the horizontal plane, respectively, and $\sigma_v$ is the vertical principal stress. Therefore, $\phi' = (\sigma_1 - \sigma_3) / (\sigma_2 - \sigma_3) = 1/\phi = 1 / (1 - R) = 1.0$–$2.0$ in the case of a strike-slip faulting stress regime. In our calculations, we assumed $R$ to be 0.3 and 0.5 for $\phi'$ of 1.5 and 2.0, respectively, because we could not uniquely determine the stress ratio around the study area.

Vertical stress ($\sigma_2$) is generally calculated as the product of $\rho$ (density), $g$ (gravitational acceleration), and $h$ (depth). We assumed $\rho = 2.7 \times 10^3$ kg/m$^3$, $g = 9.8$ m/s$^2$, and $h = 10{,}000$ m from the depth of the hypocenters, and calculated $\sigma_2$ (= $\sigma_v$) to be 264 MPa.

The mixed stress regime of strike-slip and normal faulting, determined by Matsumoto et al. (2015) from focal mechanism data, implies that $\sigma_{Hmax}$ values are very close to $\sigma_V$ ($\sigma_1 \approx \sigma_2$). However, $\sigma_V$ is not greater than $\sigma_{Hmax}$ around the source area of the 2016 Kumamoto earthquake because the fault rupture mechanism was dominantly strike-slip. Therefore, we assumed $\sigma_2/\sigma_1 = 0.9$ and $R = 0.3$, and then calculated $\sigma_1$ (= $\sigma_H$) and $\sigma_3$ (= $\sigma_h$) to be 293 and 207 MPa, respectively (Table 1). Furthermore, to determine the uncertainty of the $\sigma_1/\sigma_2$, ratio, we calculated $\sigma_1$ (= $\sigma_H$) and $\sigma_3$ (= $\sigma_h$) by assuming $\sigma_2/\sigma_1$ = 0.8 and 0.7. The resultant values of $\sigma_1$ (= $\sigma_H$) and $\sigma_3$ (= $\sigma_h$) based on $\sigma_2/\sigma_1$ = 0.8 were 330 and 110 MPa, respectively (Table 1). The results of this calculation for $\sigma_2/\sigma_1$ = 0.7 were not reasonable because the calculated $\sigma_3$ values were too low compared with those calculated with $\sigma_1/\sigma_2$ = 0.9 (Table 1). To determine the uncertainty of the stress ratio (*R*), we calculated the principal stresses in the case of *R* = 0.5 according to the same process (Table 1).

**2.2. Results of the Slip Tendency Calculations**

The Futagawa–Hinagu fault zone, which is closely related to the Median Tectonic Line, the longest and most active fault zone in Japan (Miyazaki et al., 2016), is one of the main contributors to seismic hazards on Kyushu Island (Figure 1).

In our slip tendency analysis to evaluate the seismic potential of the Futagawa–Hinagu fault zone before the 2016 Kumamoto earthquake, we examined three possible orientations of the maximum principal stress ($\sigma_1$) in the horizontal plane (N55°E, N70°E, and N85°E) and two *R* values (0.3 and 0.5) for calculating the principal stresses ($\sigma_1$, $\sigma_2$, $\sigma_3$; see section 2.1), because the slip tendency depends only on the direction of the principal stresses, *R*, and the fault model used. Here we present only the analysis results for the case of $\sigma_2/\sigma_1$ = 0.9, because variations of $\sigma_2/\sigma_1$ do not affect the slip tendency.

In this analysis, slip tendencies of the Futagawa and Hinagu fault zone sections ranged from 0.30 to 0.99, and they appeared to depend on the fault model (dip angle) and on the directions of the principal stresses (Figure 2 and Table 2). On the whole, the slip tendencies in the Hinagu fault zone seemed to be higher than those in the Futagawa fault zone.

In the Futagawa fault zone, the slip tendencies ranged widely from 0.30 to 0.92. For most calculated cases (except that with a principal stress direction of N55°E and $R$ = 0.5), the slip tendencies of the Futagawa section, which ruptured during the 2016 Kumamoto earthquake, were about 0.7 or greater. In contrast, the slip tendencies of the Uto and NCUP sections were less than 0.7 for most calculation cases, except for some of the cases with a principal stress direction of N85°E. Moreover, the slip tendencies of the Uto and NCUP sections were lower at higher dip angles, except for some of the cases with a principal stress direction of N85°E (Figure 2).

In the Hinagu fault zone, the slip tendencies of the Takano–Shirahata section, which ruptured during the 2016 Kumamoto earthquake, were roughly 0.9 for most calculation cases, except those with a principal stress direction of N85°E. The slip tendencies of the Hinagu section were greater than 0.8 for almost all of calculation cases. The slip tendencies of the Yatsushiro section were 0.9 or greater for most calculation cases, except for the two cases with the principal stress direction of N55°E.

# 3. Analysis of Seismicity before and after the 2016 Kumamoto Earthquake

## 3.1. Data

We prepared a data set extracted from the earthquake catalog maintained by the Japan Meteorological Agency (JMA) to analyze seismicity around the Kumamoto area before and after the 2016 Kumamoto earthquake. In this analysis, we used earthquakes that occurred from 1 October 1997 to 30 April 2016 around the study area (130.0°E–131.1°E, 32.1°N–33.0°N).

The completeness magnitude (*Mc*) around the study area for the JMA earthquake catalog from 1 October 1997 to 14 April 2016 (preceding the foreshock) was estimated to be 0.8 by the calculation method of Cao and Gao (2002) (Figure S2). Therefore, we extracted seismic events occurring during that period with $M_j \geq 1.0$ from the JMA earthquake catalog for the analysis of seismicity before the earthquake. For the analysis of seismicity after the earthquake, we extracted seismic events that occurred from 16 April 2016 (just after the foreshock) to 30 April 2017 with $M_j \geq 3.0$ from the JMA earthquake catalog, because of a hypocenter determination problem for seismic events with $M_j \leq 3.0$ that occurred just after the Kumamoto earthquake sequence (Zhuang et al., 2017).

Additionally, to ensure the reliability of the data from the JMA earthquake catalog, we examined hypocenter location errors. To check the data reliability of the data set that we used in the seismicity analysis, we picked out data for seismic events in 1998 and 2015 from the JMA catalog. In both of these data sets, the hypocenter location errors of 90% or more of the seismic events were within a 2 km depth range (Figure S3). Furthermore, the hypocenter location errors of 95% or more of the seismic events were within 1 km of latitude and longitude (Figure S3). These results show that the data set that we used in the seismicity analysis should be reliable enough for detection of remarkable seismicity trends within an area of several kilometers width.

### 3.2. Seismicity Analysis Method

The Futagawa and Hinagu fault zones have been a source of long-term high seismicity in the study area (e.g., Matsumoto et al., 2015). Thus, analysis of this activity might lead to a better understanding of the seismic environment within the study area.

To investigate the spatial distribution of seismicity around the hypocentral area of the 2016 Kumamoto earthquake, we used the same fault models as those used to calculate the slip tendencies. We considered seismic events that occurred at focal depths of up to 18 km within 5 km of the fault planes of the Futagawa and Hinagu fault zones (Figure 3) to be seismicity associated with those faults. The hypocenter distribution of events with $M_j \geq 1.0$ for the period before the 2016 foreshock (1 October 1997 to 14 April 2016, preceding the foreshock) and with $M_j \geq 3.0$ for the period after the 2016 foreshock (14 April 2016 to 30 April 2017, just after the foreshock) are shown in Figure 4a and 4b, respectively. Note that the hypocenter distributions related to the Uto and NCUP sections of the Futagawa fault zone are not shown in this figure, because the fault models (dip angles) of these sections cannot be estimated (see section 2.1). In this analysis, we focused on the relationship between the seismicity characteristics and the arrest of the 2016 Kumamoto earthquake rupture.

Because earthquake clusters generally complicate the estimation of seismic properties related to tectonic stress fields, we used the declustering routine (Reasenberg, 1985) in the ZMAP software package (Wiemer, 2001) to remove noise clusters from the data set. However, we were unable to determine the optimum values for two important parameters used for ZMAP declustering: taumax, the look-ahead time (days), and rfact, a factor applied to the fracture zone to determine the interaction zone (km) (rfact corresponds to Q in Reasenberg, 1985).

We tested nine combinations of the taumax and rfact declustering parameters and then extracted from the results minimum (Figure 5a), intermediate (Figure 5b), and maximum (Figure 5c) cases (cases 1, 2, and 3, respectively, in Table 3).

### 3.3. Seismic Activity Analysis Results

Many seismic events occurred within the Futagawa (Futagawa section) and Hinagu fault zones during the analysis periods (Figure 4). The spatial distribution of seismicity before the 2016 Kumamoto earthquake was heterogeneous along both fault zones. Seismic activity was clearly lower in the Yatsushiro section of the Hinagu fault zone than in the other sections of either fault zone (Figure 4a). After the 2016 Kumamoto earthquake, seismicity remained low in the Yatsushiro section, although seismicity in the other sections increased (Figure 4b).

The most remarkable characteristic of seismicity in the area around the fault zones before the 2016 Kumamoto earthquake is its heterogeneity in the Hinagu section: compared with seismicity in the central and southern parts, in the northern part of the section, seismicity was lower in a zone extending N–S for 7 km (Figure 4a). However, many aftershocks occurred in this zone (Figure 4b).

Because this low-seismicity zone was evident in all three declustering cases (Figure 5), we used the intermediate declustering result (Figure 5b) for our spatiotemporal analyses of seismicity along the Hinagu fault zone. Seismicity in the low-seismicity zone was much lower than the seismicity in the other sections (Figures 6 and 7). A moderate magnitude earthquake ($M_w$ 4.9) that occurred on 8 June 2000 in the Takano–Shirahata section of the Hinagu fault zone (Figure 4a) did not influence seismicity in the low-seismicity zone (Figure S4), even though it was located within ~5 km of the zone (Figure 4a). Moreover, another moderate earthquake ($M_w$ 4.6) on 3 June 2005, also within ~5 km of the low-seismicity zone of the Hinagu section (Figure 4a), also did not affect the seismicity of the low-seismicity zone (Figure S4). The lack of any effect of these two earthquakes on seismicity in the low-seismicity zone suggests that the zone is not sensitive to sudden seismicity changes in neighboring regions.

# 4. Evaluation of Static Stress Transfer

## 4.1. Coulomb Failure Function Analysis

In general, proximity of two earthquakes in time and space suggests that the second earthquake was triggered by stress changes caused by the first. Triggering of seismicity by large earthquakes is generally evaluated by the Coulomb failure criterion (e.g., King et al., 1994). We used Coulomb v. 3.3 stress-change software (Lin & Stein, 2004; Toda et al., 2005) to calculate Coulomb stresses imparted by the rupture of the Futagawa and Hinagu fault zones in an elastic half-space with a shear modulus of 83.3 GPa. For this calculation, we used the same source fault models that we used in the slip tendency analysis (Table S1). Coseismic displacement was calculated based on the average displacement (1.87 m) and the rake angle (142°) determined by Asano and Iwata (2016).

The static Coulomb stress change (ΔCFS) caused by a main shock is calculated as

$$\Delta CFS = \Delta\tau + \mu'\Delta\sigma_n \quad (2)$$

where $\Delta\tau$ is the shear-stress change on a given fault plane (positive in the direction of fault slip), $\Delta\sigma_n$ is the fault-normal stress change (positive for unclamping), and $\mu'$ is the apparent coefficient of friction. In this study, we set $\mu'$ to 0.4 and the Poisson ratio to 0.25, the same values we used in the slip tendency analysis. To evaluate the depth dependence of the stress perturbation, we calculated the stress perturbation at 5, 10, and 15 km depth.

To estimate the orientations of the slip planes most likely to rupture after stress perturbation due to a seismic event, the following parameters are required: (1)

directions of the principal stress axes, (2) stress ratio $R$ and principal stresses, (3) fault plane geometry, and (4) apparent friction coefficient ($\mu'$). For these parameters we used the same values as those we used in the slip tendency analysis.

### 4.2. Stress Perturbation on Kyushu Island after the 2016 Kumamoto Earthquake

The main shock of the 2016 Kumamoto earthquake perturbed stress conditions around the source faults. This fact suggests that stress perturbations can provide useful information to evaluate the earthquakes that occurred after the main shock, and then to determine where stress transfer increased the potential for slip on neighboring faults.

To evaluate the transfer of stress to the Hinagu section (Figure 8), the southwestern extension of the source faults of the 2016 Kumamoto earthquake, we assumed a receiver fault (strike/dip/rake, 215°/70°/–164.4°). The rake angle was calculated on the basis of the slip rates of the Hinagu section, which were 0.7 and 0.2 mm/y for horizontal and vertical slip rates, respectively (HERP, 2013). Stress changes on the Hinagu section due to the 2016 earthquake were positive (+11.6 to 0.0 MPa) at 10 km depth (Figure 8). The calculation results for depths of 5 and 15 km depth were similar to the calculation result for 10 km depth (Figures S5 and S6). Moreover, the stress perturbation result for a receiver fault with a different rake angle (strike/dip/rake, 215°/70°/–144.6°), calculated on the basis of horizontal and vertical slip rates of 0.7 and 0.5 mm/y, respectively, for the Hinagu section (HERP, 2013) (Figure S7) was also similar to the calculation result for a rake angle of –164.4°.

### 4.3. Optimally Oriented Fault Plane Analysis

Regional stress conditions around a fault are influenced by rupture events on neighboring faults. As a result, the orientations of the optimum slip planes around a fault are changed following rupture events on neighboring faults (King et al., 1994). King et al. (1994) analyzed Coulomb stress changes under assumed pre-earthquake stress conditions to determine the optimum slip plane orientations. To investigate the optimally oriented slip planes in our study area, we applied the methodology of King et al. (1994) to the fault models that we used in our Coulomb stress change analysis and assumed the same stress directions and ratios as those used in our slip tendency analysis (Table 1).

The pattern of Coulomb stress change calculated by taking into account regional stress conditions (Figure 9) differed from that calculated without taking them into account (Figure 8), but strong positive stress changes occurred on the receiver fault (i.e., the Hinagu section of the Hinagu fault zone) whether or not regional stress was taken into account (compare Figures 8 and 9). The strike of the southwestern extension of the source faults (the Hinagu section) is very close to the strikes of the optimum slip planes for right-lateral strike slip (Figure 9).

In the case of an $\sigma_1$ orientation of N55°E, the fault strike of the Hinagu section crossed the optimum plane orientation at an oblique angle (Figure S8a), whereas with an $\sigma_1$ orientation of N85°E or N70°E, the fault strike of the Hinagu section was roughly parallel to the optimum plane orientation (Figures S8b and 9). The Coulomb stress change pattern was similar among these three $\sigma_1$ orientation cases. Additionally, the calculation results were roughly the same even when different stress ratios ($R$ = 0.3 and 0.5) and $\sigma_2/\sigma_1$ values ($\sigma_2/\sigma_1$ = 0.8 and 0.9) were used (Figures 9, S9, and S10).

# 5. Discussion

### 5.1. Seismic Potential of the Futagawa–Hinagu Fault Zone before the 2016 Kumamoto Earthquake

The slip tendencies of the sections of the Futagawa and Hinagu fault zones ranged widely from 0.30 to 0.99 (Figure 2 and Table 2). Overall, the slip tendencies of the three sections in the Futagawa fault zone were lower than those of the three sections in the Hinagu fault zone. More specifically taking the principal stress directions reported by Matsumoto et al, (2015), the $\sigma_1$ orientation of N70°E should be appropriate for the three sections of the Futagawa fault zone and the Takano–Shirahata and Hinagu sections of the Hinagu fault zone. In addition, the $\sigma_1$ orientation of N85°E and N55°E seems to be more suitable to the northern part from Mt. Aso and the Yatsushiro section, respectively. Following the consideration, in the Futagawa fault zone, the slip tendencies calculated for the Futagawa section, one of the source faults of the 2016 Kumamoto earthquake, tended to be higher than those calculated for the other sections (Table 2). In the Hinagu fault zone, the slip tendencies of the Takano–Shirahata and Hinagu sections were mostly high (≥ 0.8), however the Yatsushiro section showed low slip tendencies (0.4). Therefore, the seismic potentials of the Futagawa section in the Futagawa fault zone and of the Takano–Shirahata and Hinagu sections in the Hinagu fault zone were high before the 2016 Kumamoto earthquake. These results are consistent with the occurrences of the foreshock and main shock of the 2016 Kumamoto earthquake on the Takano–Shirahata section in the Hinagu fault zone and on the Futagawa section in the Futagawa fault zone, respectively.

Many studies have presented empirical evidence based on earthquake data that discontinuities in faults or fault zones are closely related to the initiation and arrest of fault rupture (Biasi & Wesnousky, 2016; King, 1986; King & Nabelek, 1985;

Wesnousky, 2006). Moreover, Nakano et al. (2010) showed by numerical modeling that stress increases at fault discontinuities can occur both interseismically and coseismically, and that stress may not be released unless new fractures are created. These study results indicate that heterogeneous stress states that develop in regions around fault discontinuities lead to both initiation and arrest processes of fault rupture propagation. The hypocenter of the 2016 Kumamoto earthquake foreshock was located on the Takano–Shirahata section of the Hinagu fault zone, near the intersection of the Hinagu and Futagawa fault zones. Matsumoto et al. (2018) reported that the pre-earthquake stress state in the region around the hypocenter of the 2016 Kumamoto earthquake, estimated by using earthquake moment tensor data, was heterogeneous, and that the fault rupture propagation during the earthquake was correspondingly heterogeneous. These facts suggest that the heterogeneous stress condition in the region around the hypocenter of the 2016 Kumamoto earthquake before the earthquake set the stage for the initiation of fault rupture. Taking this pre-earthquake heterogeneity into consideration, we might infer that the Takano–Shirahata section was more likely to rupture than the Hinagu section in the Hinagu fault zone. However, the slip tendency calculation results showed that the two sections of the Hinagu fault zone had high seismic potential before the earthquake.

Paleoseismological data can also provide important information about fault rupture initiation and propagation processes. The available paleoseismological data for the Futagawa and Hinagu fault zones, based on HERP (2019), are summarized in Table 4. Unfortunately, few paleoseismological data for the Uto section, and none for the NCUP section, of the Futagawa fault zone are available. Additionally, no data are available for the penultimate events in the Takano–Shirahata section and low-seismicity zone of the

Hinagu fault zone. However, data on the timing of the latest rupture event and the average recurrence interval of the Futagawa section of the Futagawa fault zone and of the three sections of the Hinagu fault zone are available.

We used the available paleoseismological data (Table 4) to calculate the 30-year exceedance probability ($P$) for each section of the two fault zones before the 2016 Kumamoto earthquake. We used the Poisson process,

$$P\,(T, \Delta T) = 1 - e^{-\Delta T/T} \qquad (3)$$

where $T$ is average recurrence interval and $\Delta T$ was set to 30 years, to evaluate the seismic potential of each fault section (Figure 10).

The rupture probabilities (1.0–1.5%) obtained for the Futagawa section, one of the source faults of the 2016 Kumamoto earthquake, were highest among all sections of the Futagawa fault zone. The rupture probabilities of the Takano–Shirahata and Yatsushiro section in the Hinagu fault zone, 1.2% and 1.4%, respectively, were also high. In contrast, the rupture probabilities of the Hinagu section were low, 1.0% and 0.7% in the low-seismicity zone and the southern part of the Hinagu section, respectively, in comparison with the other sections of the Hinagu fault zone. Given that the rupture probability of the Takano–Shirahata section was roughly the same or only a little lower than that of the Yatsushiro section, the stress heterogeneity around the earthquake hypocenter must have primed the initiation of the fault rupture. In addition, the slip tendencies of the Yatsushiro section were low. Therefore, before the 2016 Kumamoto earthquake, the seismic potential of the two source fault sections, the Takano–Shirahata section of the Hinagu fault zone and the Futagawa section of the Futagawa fault zone, of the 2016 Kumamoto earthquake was high enough for them to rupture in comparison with other fault sections of the two fault zones.

## 5.2. Interruption of Rupture Propagation to the Southwest during the 2016 Kumamoto Earthquake

The rupture histories of the three sections of the Hinagu fault zone are different (Table 4). In particular, the average recurrence interval on the southern part of the Hinagu section is far longer than that in the low-seismicity zone. The rupture probabilities were also different among the three sections of the Hinagu fault zone (Figure 10). These facts suggest that rupture conditions differ among the three sections. It is noteworthy that the rupture probability of the southern part of the Hinagu section was lowest among the Hinagu fault zone sections. The different rupture conditions probably affected the rupture propagation from the Takano–Shirahata section toward the Hinagu section.

Seismicity in general and the propagation of rupture along faults in particular are influenced by geological barriers such as complex geological structures and locked faults (Bohnfoff et al., 2013). The geological structure in and around our study area is complicated. The surface geology of central Kyushu Island is characterized by several fault-bounded belts in a zonal arrangement. Two major terrane boundary faults, the Usuki–Yatsushiro Tectonic Line (UYTL) and the Butsuzo Tectonic Line (BTL) (Miyazaki et al., 2016), intersect the Hinagu fault zone (Figure 11). North of the UYTL, the rocks are dominantly of pre-Jurassic and Cretaceous age, whereas those between the UYTL and BTL are mainly of pre-Jurassic and Jurassic age. Rocks to the south of the BTL belong to a Cretaceous accretionary complex. The intersection of the Hinagu fault zone with the UYTL is in the Hinagu section, and it roughly coincides with the southern limit of the low-seismicity zone (Figure 11). North of the intersection, the

Hinagu fault zone is in pre-Jurassic to Jurassic and Cretaceous rocks. However, low-P/T metamorphic and granitic rocks of the Higo metamorphic complex also occur close to the intersection, and their distribution coincides roughly with the low-seismicity zone of the Hinagu section (Figure 11). Matsumoto et al. (2016) reported that a remarkable gravity anomaly exists in the Hinagu section. The boundary of the gravity anomaly corresponds to the structural boundary between the Hinagu section and the Takano–Shirahata section, which is attributable to a geological boundary related to the distribution of the Higo metamorphic rocks. They suggested that this structural boundary played an important role in controlling the spatial extent of the source faults of the 2016 Kumamoto earthquake.

Our seismic analysis results suggest the existence of a remarkable low-seismicity zone in the northern part of the Hinagu section, and the rupture histories are different among the three sections and the low-seismicity zone of the Hinagu fault zone. Given that heterogeneous geological structures are closely related to rupture conditions and seismic activity on each fault section, the combined effect of the presence of the highly rigid Higo metamorphic complex and the intersection of two major faults probably accounts for the curtailment of the rupture propagation from the source faults of the 2016 Kumamoto earthquake to the southwest. This interpretation is supported by the results of our seismic activity analysis (section 3.3) showing that the low-seismicity zone was not sensitive to nearby (within ~5 km) moderate magnitude seismic events.

### 5.3. Seismic Potential in the Hinagu fault zone

Although the southward rupture propagation of the source faults of the 2016 Kumamoto earthquake was curtailed by the low-seismicity zone, the high slip tendency

(Figure 2) and the positive stress change (Figure 8) after the 2016 Kumamoto earthquake of the Hinagu section, together with the consistency of the optimum slip planes with the fault strike of the Hinagu fault (Figure 9), indicate a high potential for future earthquakes along the Hinagu section that are related to the 2016 Kumamoto earthquake.

The spatial distribution of viscous properties plays a key role in earthquake triggering (e.g., Freed & Lin, 2001). Analyses of geodetic data reveal that viscoelastic relaxation of the lower crust and mantle occurred following the 2016 Kumamoto earthquake (Pollitz et al., 2017; Moore et al., 2017; Fuwa & Ohzono, 2018). Moreover, Pollitz et al. (2017) indicated that the postseismic relaxation in the near field (within 30 km of the main shock epicenter) was dominantly from afterslip, whereas at greater distance viscoelastic relaxation was dominant. The aftershock distribution of the 2016 Kumamoto earthquake shows that the region of postseismic relaxation corresponds to the northern part of the Hinagu section (the low-seismicity zone) (Figures 4b and 5). Additionally, Nanjo et al. (2019) reported the existence of a high-stress area at the southern end of the source faults, including in the postseismic relaxation region, after the 2016 Kumamoto earthquake. Rupture nucleation is likely to occur eventually in highly stressed areas. In addition, because a similar highly stressed area was observed before the main shock of the 2016 Kumamoto earthquake (Nanjo et al., 2016), the stress concentration region is regarded as a candidate location for the initiation of future earthquake ruptures. Because stress in the Takano–Shirahata section and the low-seismicity zone of the Hinagu fault zone was relaxed by an afterslip, a future rupture would be expected to propagate along the remaining southern section. Therefore, the seismicity and geodetic analysis results also indicate, in agreement with our research results, that the southern part of the Hinagu section is under high stress and has potential for future rupture.

## 6. Conclusions

The main events of the 2016 Kumamoto earthquake were a foreshock ($M_w$ 6.2) on 14 April and the main shock ($M_w$ 7.0) on 16 April 2016, both of which were caused by fault ruptures near the intersection of the Futagawa and Hinagu fault zones. We considered the rupture process and the potential for future earthquakes within those fault zones from the viewpoint of structural geology, seismicity data, and paleoseismological data, and by using numerical analyses. Taking into consideration the regional fault geometry, slip tendency analysis results, and the fault rupture history, we concluded that the rupture potential of the source faults of the 2016 Kumamoto earthquake was high before the earthquake. Further, the seismicity and southwestward rupture propagation after the earthquake were probably controlled by geological heterogeneities of the fault zones. However, our analysis of the Coulomb stress change during the 2016 earthquake revealed a positive stress change on the northern part of the Hinagu section close to the Takano–Shirahata section after the earthquake, and an optimum slip plane orientation that was consistent with the fault strike of the Hinagu section. Furthermore, in addition to the high slip tendency of the Hinagu section, postseismic deformation led to a stress concentration at the southern end of the source faults, including in the afterslip region of the 2016 Kumamoto earthquake. These results, by providing crucial information about the likelihood of future earthquakes in the region of the 2016 Kumamoto earthquake, can contribute to preparations for future earthquake disaster mitigation.

**Acknowledgments**

We thank the Japan Meteorological Agency for the use of their earthquake catalog (http://www.jma.go.jp/jma/indexe.html) and the Japanese National Institute for Earth Science and Disaster Prevention for providing focal mechanism data (http://www.fnet.bosai.go.jp/top.php?LANG=en). We also thank Ms. Fumiko Suzuki, Shikoku Research Institute Inc., for drawing some of the figures in this paper. We are grateful to the editor Rachel Abercrombie and two anonymous reviewers for their helpful comments on our manuscript. Some figures were prepared by using the Generic Mapping Tools software package (Wessel & Smith, 1998).

## References


Asano, K., & Iwata, T. (2016). Source rupture process of the foreshock and mainshock in the 2016 Kumamoto earthquake sequence estimated from the kinematic waveform inversion of strong motion data. *Earth Planets Space*, 68. https://doi:10.1186//s40623-016-0519-9

Biasi, G. P., & Wesnousky, S. G. (2016). Steps and gaps in ground ruptures: Empirical bounds on rupture propagation. *Bulletin of the Seismological Society of America*, 106, 1110–1124. https://doi: 10.1785/0120150175

Bohnfoff, M., Bulut, F., Dressen, G., Malin, P. T., Eken ,T., & Aktar, M. (2013). An earthquake gap south of Istanbul. *Nature Communications*, 4:1999 doi: 10.1038/ncomms2999.

Bos, B., & Spiers, C. J. (2002). Friction-viscous flow of phyllosilicate-bearing fault rock: Microphysical model and implications for crustal strength profiles. *Journal of Geophysical Research*, 107, B2, 2028. https://doi.org/10.1029/2001JB000301.

Byerlee, J. (1978). Friction of rocks. *Pure and Applied Geophysics (PAGEOPH)*, 116, 615–627.

Cao, A., & Gao, S. S. (2002). Temporal variation of seismic b-values beneath northeastern Japan island arc. *Geophysical Research Letters*, 29, doi.org/10.1002/2016GL070079.

Freed, A. M., & Lin, J. (2001). Delayed triggering of the 1999 Hector Mine earthquake by viscoelastic stress transfer. *Nature*, 411(6834), 180–183.

Fukahata, Y., & Hashimoto, M. (2016). Simultaneous estimation of the dip angles and slip distribution on the faults of the 2016 Kumamoto earthquake through a weak nonlinear inversion of InSAR data. *Earth Planet Space*, 68, 204.

https://doi.org/10.1186//s40623-016-0580-4.

Fuwa, S., & Ohzono, M. (2018). Viscosity distribution beneath the Kyushu Island estimated by GNSS postseismic time series of the 2016 Kumamoto earthquake (*M*7.3) (in Japanese with English abstract). *Geophysical Bulletin of Hokkaido University*, 81, 45–55. https://doi.org/10.14943/gbhu.81.45.

Geospatial Information Authority of Japan. (2016). Fault model of the 2016 Kumamoto earthquake (preliminary). http://www.gsi.go.jp/common/000140781.pdf, accessed 2 March, 2017.

Headquarters for Earthquake Research Promotion. (2013). Regional evaluation for active faults in Kyushu: Futagawa and Hinagu Fault zones. http://jishin.go.jp/main/chousa/katsudansou_pdf/93_futagawa_hinagu_2.pdf, accessed 4 September, 2020.

Headquarters for Earthquake Research Promotion. (2019). Active fault research following the 2016 Kumamoto earthquakes, https://www.jishin.go.jp/main/chousakenkyuu/kumamoto_sogochousa/h28-h30/h28-h30kumamoto_sogochousa_3_1.pdf, accessed 4 September, 2020.

Kato, A., Fukuda, J., Nakagawa, S., & Okada, K. (2016). Foreshock migration preceding the 2016 *Mw* 7.0 Kumamoto earthquake, Japan. *Geophysical Research Letters*, 43, https://doi.org/10.1002/2016GL070079.

King, G. C. P. (1986). Speculations on the geometry of the initiation and termination processes of earthquake rupture and its relation to morphology and geological structure. *Pure and Applied Geophysics (PAGEOPH)*, 124, 567–585. https://doi.org/10.1007/BF00877216.

King, G. C. P., & Nabelek, J. (1985). Role of fault bends in the initiation and termination of earthquake rupture. *Science*, 228, 984–987. https://doi.org/10.1126/science.228.4702.984.

King, G. C. P., Stein, R. S., & Lin, J. (1994). Static stress changes and the triggering of earthquakes. *Bulletin of the Seismological Society of America*, 84, 935–953.

Kobayashi, T. (2017). Earthquake rupture properties of the 2016 Kumamoto earthquake foreshocks ($M_j$ 6.5 and $M_j$ 6.4) revealed by conventional and multiple-aperture InSAR. *Earth Planet Space,* 69, 7. https://doi.org/10.1186//s40623-016-1594-y.

Lin, R. J., & Stein, R. S. (2004). Stress triggering in thrust and subduction earthquakes, and stress interaction between the southern San Andreas and nearby thrust and strike-slip faults. *Journal of Geophysical Research*, 109, B2, 0303. https://doi.org/10.1029/2003JB002607.

Lisle, R. J., & Srivastava, D. C. (2004). Test of the frictional reactivation theory for faults and validity of fault-slip analysis. *Geology*, 32, 569–572. https://doi.org/10.1130/G20408.1.

Matsumoto, N., Hiramatsu, Y., & Sawada, A. (2016). Continuity, segmentation and faulting type of active fault zones of the 2016 Kumamoto earthquake inferred from analyses of a gravity gradient tensor. *Earth Planets Space*, 68:167, DOI 10.1186/s40623-016-0541-y.

Matsumoto, S., Nakao, S., Ohkura, T., Miyazaki, M., Shimizu, H., Abe, Y., et al. (2015). Spatial heterogeneities in tectonic stress in Kyushu, Japan and their relation to a major shear zone. *Earth Planet Space*, 67:172, DOI 10.1186/s40623-015-0342-8.

Matsumoto, S., Yamashita, Y., Nakamoto, M., Miyasaki, M., Sakai, S., Iio, Y., et al. (2018). Prestate of stress and fault behavior during the 2016 Kumamoto earthquake

(*M*7.3). *Geophysical Research Letters*, 45, 637–645. https://doi.org/10.1002/2017GL075725.

Miyazaki, K., Ozaki, M., Saito, M., & Toshimitsu, S. (2016). The Kyushu–Ryukyu Arc. In: Moreno, T., Wallis, S., Kojima, T. & Gibbons, W. (Eds) *The Geology of Japan* (pp. 139–174), The Geological Society, London.

Moore, J. D. P., Yu, H., Tang, C.-H., Wang, T., Barbot, S., Peng, D., et al. (2017). Imaging the distribution of transient viscosity after the 2016 *M*w 7.1 Kumamoto earthquake. *Science*, 356(6334), 163–167. https://doi.org/10.1126/science.aal3422.

Morris, A., Ferril, D. A., & Hon, D.B. (1996). Slip-tendency analysis and fault reactivation. *Geology*, 24, 275–278. https://doi.org/10.1130/0091-7613(1996)024<0275:STAAFR>2.3.CO;2

Morrow. C., Radney, B., & Byerlee, J. (1992). Frictional strength and the effective pressure law of montmorillonite and illite clays, *International. Geophysics*, 51, 69–88.

Nakano, M., Kumagai, H., Toda, S., Ando, R., Yamashina, T., Inoue, H., & Sunarjo (2010). Source model of an earthquake doublet that occurred in a pull-apart basin along the Sumatran fault, Indonesia. *Geophysical Journal International*, 181, 141–153.

Nanjo, K. Z., Izutsu, J., Orihara, Y., Furuse, N., Togo, S., Nitta, H., Okada, T., Tanaka, R., Kamogawa, M., & Nagao, T. (2016). Seismicity prior to the 2016 Kumamoto earthquakes. *Earth Planets Space*, 68, 187, doi:10.1186/s40623-016-0558-2.

Nanjo, K. Z., Izutsu, J., Orihara, Y., Kamogawa, M., & Nagao, T. (2019). Changes in seismicity pattern due to the 2016 Kumamoto earthquakes identify a highly stressed area on the Hinagu fault zone. *Geophysical Research Letters*, 46, 9489–

9496. https://doi.org/10.1029/2019GL083463.

Neves, M. C., Paiva, L. T., & Luis, J. (2009). Software for slip-tendency analysis in 3D: A plug-in for Coulomb. *Computers & Geosciences,* 35, 2345–2352.

Niemeijer, A. R., & Spiers, C. J. (2005). Influence of phyllosilicates on fault strength in the brittle–ductile transition: insights from rock analogue experiments. In Bruhn, D. & Burline, L. (Eds.), *High-strain zones: Structure and Physical Properties. Geological Society of London, Special Publications* (Vol. 245, pp. 303–327), The Geological Society, London.

Pollitz, F. F., Kobayashi, T., Yarai, H., Shibazaki, B., & Matsumoto T. (2017). Viscoelastic lower crust and mantle relaxation following the 14–16 April 2016 Kumamoto, Japan, earthquake sequence. *Geophysical Research Letters*, 44, 8795–8803. doi:10.1002/2017GL074783.

Reasenberg, P. (1985). Second-order moment of central California seismicity, 1969–1982. *Journal of Geophysical Research*, 90, B7, 5479–5495.

Shirahama, Y., Yoshimi, M., Awata, Y., Maruyama, T., Azuma, T., Miyashita, Y., et al. (2016). Characteristics of the surface ruptures associated with the 2016 Kumamoto earthquake sequence, central Kyushu, Japan. *Earth Planet Space*, 68, 191. https://doi.org/10.1186//s40623-016-0559-1.

Sugito, N., Goto, H., Kumahara, Y., Tsutsumi, H., Nakata, T., Kagohara, K., et al. (2016). Surface fault ruptures associated with the 14 April foreshock ($M_j$ 6.5) of the 2016 Kumamoto earthquake sequence, southwest Japan. *Earth Planet Space*, 68, 170. https://doi.org/10.1186//s40623-016-1547-5.

Toda, S., Kaneda, H., Okada, S., Ishimura, D., & Mildon, Z. K. (2016). Slip-partitioned surface ruptures for the $M_w$ 7.0 16 April 2016 Kumamoto, Japan, earthquake, *Earth*

*Planet Space*, 68, 188. https://doi.org/10.1186//s40623-016-0560-8.

Toda, S., Stein, R. S., Richards-Dinger, K., & Bozkurt, S., (2005). Forecasting the evolution of seismicity in southern California: Animations built on earthquake stress transfer. *Journal of Geophysical Research*, 110, B05S16, https://doi.org/1029/2004/JB003415.

Uchide, T., Horikawa, H., Nakai, M., Matsushita, R., Shigematsu, N., Ando, R., & Imanishi, K. (2016). The 2016 Kumamoto–Oita earthquake sequence: aftershock seismicity gap and dynamic triggering in volcanic areas, *Earth Planet Space*, 68, 180. https://doi.org/10.1186//s40623-016-0556-4.

Wesnousky, S. G. (2006). Predicting the endpoints of earthquake ruptures, *Nature*, 444, 358-360. https://doi.org/10.1038/nature05275.

Wessel, P., & W. H. F. Smith (1998), New improved version of Generic Mapping Tools released, *EOS Trans. AGU*, 79, 579.

Wiemer, S. (2001). A software package to analyze seismicity: ZMAP, Seismological Research Letters, 72, 2.

Yano, T. E., & Matsubara, M. (2017). Effect of newly refined hypocenter locations on the seismic activity recorded during the 2016 Kumamoto Earthquake sequence, *Earth Planets Space*, 69:74, DOI 10.1186/s40623-017-0656-9.

Zhuang, J., Ogata, Y., & Wang, T. (2017). Data completeness of the Kumamoto earthquake sequence in the JMA catalog and its influence on the estimation of the ETAS parameters, *Earth Planets Space*, 69:36, DOI 10.1186/s40623-017-0614-6.

**Table titles and figure captions**

Table 1. Stress conditions used to calculate slip tendencies and orientation of optimum slip planes. *R*, Stress ratio. $\sigma_1$ and $\sigma_2$, Maximum and moderate principal stresses. $\sigma_H$ and $\sigma_h$, Maximum and minimum horizontal stresses. $\sigma_v$, Vertical stress.

Table 2. Calculation results of slip tendencies of the Futagawa and Hinagu fault zones. There are uncertainties for the direction of the maximum principal stress ($\sigma_1$) and stress ratio (*R*). N55°E, N70°E, and N85°E are assumed for $\sigma_1$ directions. The stress ratios (*R*) are assumed to be 0.3 and 0.5. Furthermore, 40°, 70°, and 90° are assumed for dip angles of the Uto and North coast of Uto Peninsula (NCUP) sections of the Futagawa sections, because of no previously reported data.

Table 3. Parameters and results of the three cases of declustering.

Table 4. Paleoseismological data of the Futagawa fault zone and the Hinagu fault zone. Those data are summarized on the basis of HERP (2013, 2019).

Figure 1. Regional (inset) and local (main) map showing the tectonic framework of the Kyushu region, Japan. Epicenters and focal mechanisms of the foreshock (green star and beach ball) and main shock (red star and beach ball) of the 2016 Kumamoto earthquake are shown (from the NIED F-net Broadband Seismograph Network). Earthquakes ($M_j \geq 3$) with focal depth of less than 18 km between 14 April 2016 and 30 April 2017 are also shown (from the JMA earthquake catalog). Takano–Shirahata (T–S), Hinagu, and Yatsushiro sections of the Hinagu fault zone (Hg Fz) are shown. The Futagawa (Ft), Uto, and Northern coast of Uto Peninsula (NCUP) sections are shown for the Futagawa

fault zone (Ft Fz). MTLFZ, Median Tectonic Line fault zone; EU, Eurasia plate; PHS, Philippine Sea plate; PA, Pacific plate; NA, North America plate. Red lines are active faults. Blue dashed lines mark the Usuki–Yatsushiro Tectonic Line (after Miyazaki et al., 2016).

Figure 2. 3-D view of slip tendencies (*Ts′*; color scale) before the 2016 Kumamoto earthquake for the active faults included in this analysis. The direction of the maximum principal stress ($\sigma_1 = \sigma_H$) is assumed to be N70°E. The apparent friction coefficient ($\mu'$) and Poisson ratio are 0.4 and 0.25, respectively. The stress condition to calculate is assumed on the basis of $\sigma_2/\sigma_1$ = 0.9 and a stress ratio = 0.3. The maps show the calculation results depending on the dip angles of the Uto and NCUP sections. (a) 40°, (b) 70° (c) 90°. T–S, Takano–Shirahata section; Hg, Hinagu section; Ys, Yatsushiro section; Ut, Uto section; NCUP, Northern Coast of Uto Peninsula section; Ys, Yatsushiro section. See Table 2 for calculation results of other cases.

Figure 3. Schematic illustration of the method used to identify seismic events within 5 km of a fault plane. (a) Plain view of fault plane (red) and 5 km limit (blue) and (b) cross section A–B (location in panel a). Most seismic events selected are within 5 km on either side of the fault. The upper and lower depth limits for selected events are 0 and 18 km, respectively.

Figure 4. Hypocenter distribution ($M_j \geq 1$) of events associated with faults of the Futagawa (Futagawa section) and Hinagu fault zones that occurred between (a) 1 October 1997 and 14 April 2016 preceding the foreshock of the 2016 Kumamoto earthquake. (b) Hypocenter distribution ($M_j \geq 3$) of events associated with faults of the Futagawa and Hinagu fault zones that occurred

between 14 April 2016 just after the foreshock and 30 April 2017, selected as described in Figure 3. Data are from the JMA earthquake catalog. Blue solid quadrangles indicate the areal extents of fault planes used in this study. Blue dashed quadrangles are not used in the analysis. Hypocenters and focal mechanisms for the 2000 ($M_w$ 4.9) and 2005 ($M_w$ 4.6) earthquakes are also shown from the JMA earthquake catalog and the NIED F-net Broadband Seismograph Network. Abbreviations of the sections of the Futagawa and Hinagu fault zones are as in Figure 1.

Figure 5. Spatiotemporal evolution (from 1 October 1997 to 30 April 2017 in the JMA earthquake catalog) of seismicity ($M_j \geq 1$: from 1 October 1997 to 14 April 2016 preceding the foreshock, and $M_j \geq 3$: from 14 April 2016 just after the foreshock to 30 April 2017) in the Hinagu fault zone based on declustering results of three cases using two parameters (taumax and rfact). Focal depth limits of seismic events along each section depend on fault models of each fault section in Table S1. (a) Taumax and rfact are 2 and 2, respectively, (b) taumax and rfact are 5 and 5, respectively, (c) taumax and rfact are 10 and 10, respectively. Red quadrangles indicate the areal extent of the fault planes used in this study. Red dashed quadrangles are not used in the analysis. Red dashed lines show the limits of the low-seismicity zone. 08/Jun/2000 and 03/Jun/2005 show the event times for the 2000 ($M_w$ 4.9) and 2005 ($M_w$ 4.6) earthquakes, respectively.

Figure 6. Time series of earthquakes after declustering by taumax 5 and rfact 5 between 1 October 1997 and 30 April 2017 from JMA earthquake catalog ($M_j$ $\geq 1$: from 1 October 1997 to 14 April 2016 preceding the foreshock, and $M_j \geq$

3: from 14 April 2016 just after the foreshock to 30 April 2017) for each section of the Hinagu fault zone and for the low-seismicity zone identified in this study. 08/Jun/2000 and 03/Jun/2005 show the event times for the 2000 ($M_w$ 4.9) and 2005 ($M_w$ 4.6) earthquakes, respectively. Time series of earthquakes without declustering are shown in Figure S4.

Figure 7. M–T diagrams for each section from 1 October 1997 to 30 April 2017 in JMA earthquake catalog ($M_j \geq 1$: from 1 October 1997 to 14 April 2016 preceding the foreshock, and $M_j \geq 3$: from 14 April 2016 just after the foreshock to 30 April 2017). (a) Takano–Shirahata section, (b) Hinagu section, (c) Yatsushiro section, (d) Low-seismicity zone. 08/Jun/2000 and 03/Jun/2005 show the event times for the 2000 ($M_w$ 4.9) and 2005 ($M_w$ 4.6) earthquakes, respectively.

Figure 8. Coulomb stress perturbation due to the 2016 Kumamoto earthquake. Red rectangles show each fault model. The fault models are recreated based on Asano & Iwata (2016) and HERP (2013) (Table S1). Green and black lines show the surface and 10 km depth traces for each fault model, respectively. The receiver fault (strike/dip/rake, 215°/70°/–164.4°) is used to evaluate stress changes on the faults of the Hinagu fault zone. (a) Regional view of the Coulomb stress perturbation, (b) enlarged view of the Coulomb stress perturbation. Annotated numerals are stress changes at selected points (white-filled circles) on the faults. Grid size for calculation is 2 × 2 km. Yellow and blue fault lines represent the rupture and receiver faults, respectively. Abbreviations of the sections of the Futagawa and Hinagu fault zones are as presented in Figure 1. The calculation results at 5 and 15 km are

shown in Figures S5 and S6, respectively. And Coulomb stress perturbation for another receiver fault (strike/dip/rake, 215°/70°/–144.6°) is shown in Figure S7.

Figure 9. Coulomb stress perturbation and optimum slip planes for the orientation of the regional stress field. The regional stress condition is the same as it used for the slip tendency analysis ($\sigma_1$ direction: N70°E, $\sigma_2/\sigma_1$ = 0.9 and a stress ratio = 0.3), and the fault models follow the Coulomb stress change analysis (Table S1). Red rectangles, green and black lines are same as in Figure 8. Grid size for calculation is about 5 × 5 km. Yellow fault lines represent rupture faults. Abbreviations of the sections of the Futagawa and Hinagu fault zones are as presented in Figure 1. The calculation results for the $\sigma_1$ direction of N55°E and N85°E are shown Figure S8. The calculation results for the stress ratio of 0.5 and 0.7 are shown in Figure S9. The calculation results for the $\sigma_2/\sigma_1$ = 0.7 and 0.8 are show in Figure S10.

Figure 10. 30-years exceedance probabilities for each section of the two fault zones. See text for detail.

Figure 11. Relationship between geology and seismicity around the Futagawa and Hinagu fault zones. Hypocenter distribution of events is same as Figure 4a. Base geological map is from GeomapNavi (https://gbank.gsj.jp/geonavi/).

| direction of $\sigma_1$ | $R$ | $\sigma_2/\sigma_1$ | $\sigma_1 = (\sigma_H)$ | $\sigma_2 = (\sigma_v)$ | $\sigma_3 = (\sigma_h)$ |
|---|---|---|---|---|---|
| N55°E | 0.3 | 0.9 | 293.0 | 264.0 | 207.0 |
| | | 0.8 | 330.0 | 264.0 | 110.0 |
| N70°E | | 0.7 | 377.0 | 264.0 | 0.3 |
| | 0.5 | 0.9 | 293.0 | 264.0 | 235.0 |
| N85°E | | 0.8 | 330.0 | 264.0 | 198.0 |
| | | 0.7 | 377.0 | 264.0 | 151.0 |

| | $\sigma_1$ = N55°E | | | | | | $\sigma_1$ = N70°E | | | | | | $\sigma_1$ = N85°E | | | | | |
|---|---|---|---|---|---|---|---|---|---|---|---|---|---|---|---|---|---|---|
| | *R* = 0.3 | | | *R* = 0.5 | | | *R* = 0.3 | | | *R* = 0.5 | | | *R* = 0.3 | | | *R* = 0.5 | | |
| *Futagawa fault zone* | | | | | | | | | | | | | | | | | | |
| Futagawa | 0.69 | | | 0.51 | | | 0.80 | | | 0.69 | | | 0.91 | | | 0.88 | | |
| | Dip (°) | | | Dip (°) | | | Dip (°) | | | Dip (°) | | | Dip (°) | | | Dip (°) | | |
| | 40 | 70 | 90 | 40 | 70 | 90 | 40 | 70 | 90 | 40 | 70 | 90 | 40 | 70 | 90 | 40 | 70 | 90 |
| Uto | 0.69 | 0.66 | 0.35 | 0.55 | 0.53 | 0.35 | 0.68 | 0.67 | 0.40 | 0.55 | 0.55 | 0.40 | 0.67 | 0.90 | 0.90 | 0.67 | 0.86 | 0.90 |
| North coast of Uto Peninsula | 0.69 | 0.65 | 0.30 | 0.55 | 0.51 | 0.30 | 0.68 | 0.69 | 0.44 | 0.55 | 0.57 | 0.44 | 0.67 | 0.91 | 0.92 | 0.67 | 0.87 | 0.92 |

| | $\sigma_1$ = N55°E | | $\sigma_1$ = N70°E | | $\sigma_1$ = N85°E | |
|---|---|---|---|---|---|---|
| | *R* = 0.3 | *R* = 0.5 | *R* = 0.3 | *R* = 0.5 | *R* = 0.3 | *R* = 0.5 |
| *Hinagu fault zone* | | | | | | |
| Takano–Shirahata | 0.94 | 0.92 | 0.87 | 0.87 | 0.64 | 0.66 |
| Hinagu | 0.83 | 0.77 | 0.94 | 0.93 | 0.83 | 0.84 |
| Yatushiro | 0.40 | 0.40 | 0.90 | 0.90 | 0.99 | 0.99 |

| | case 1 | case 2 | case 3 |
|---|---|---|---|
| taumax | 2 | 5 | 10 |
| rfact | 2 | 5 | 10 |
| number of clusters (a) | 617 | 11 | 9 |
| number of declustered earthquakes (b) | 3,232 | 25 | 71 |
| number of independet earthquakes (c) | 1,756 | 1,742 | 1,680 |
| b+c-a | 4,371 | 1,756 | 1,742 |
| number of earthquakes within 5 km on each fault plane of three sections | | | |
| Takano-Shirahata | 743 | 655 | 609 |
| Hinagu | 1,155 | 1,060 | 1,013 |
| Yatsushiro | 303 | 301 | 298 |

| | latest rupture event | penultimate event | average recurrence interval |
|---|---|---|---|
| *Futagawa fault zone* | | | |
| Futagawa section | 1800 – 1700 y. BP | 5600 – 4500 y. BP | 2000 – 3000 years |
| Uto section | 15760 – 9550 (or 2750) | n. d. | n. d. |
| Northern Coast of Uto Peninsula section (NCUP) | n. d. | n. d. | n. d. |
| *Hinagu fault zone* | | | |
| Takano – Shirahata section | 1400 – 1100 y.BP | n. d. | 2400 – 2500 years |
| Hinagu section | low-seismicity zone 1900 – 1100 y. BP | n. d. | low-seismicity zone 3000 years |
| | 3100 – 2000 y. BP | 7300 – 7000 y. BP | 4250 years |
| Yatsushiro section | 1600 y. BP | n. d. | 2100 years |

**Figure 1.**

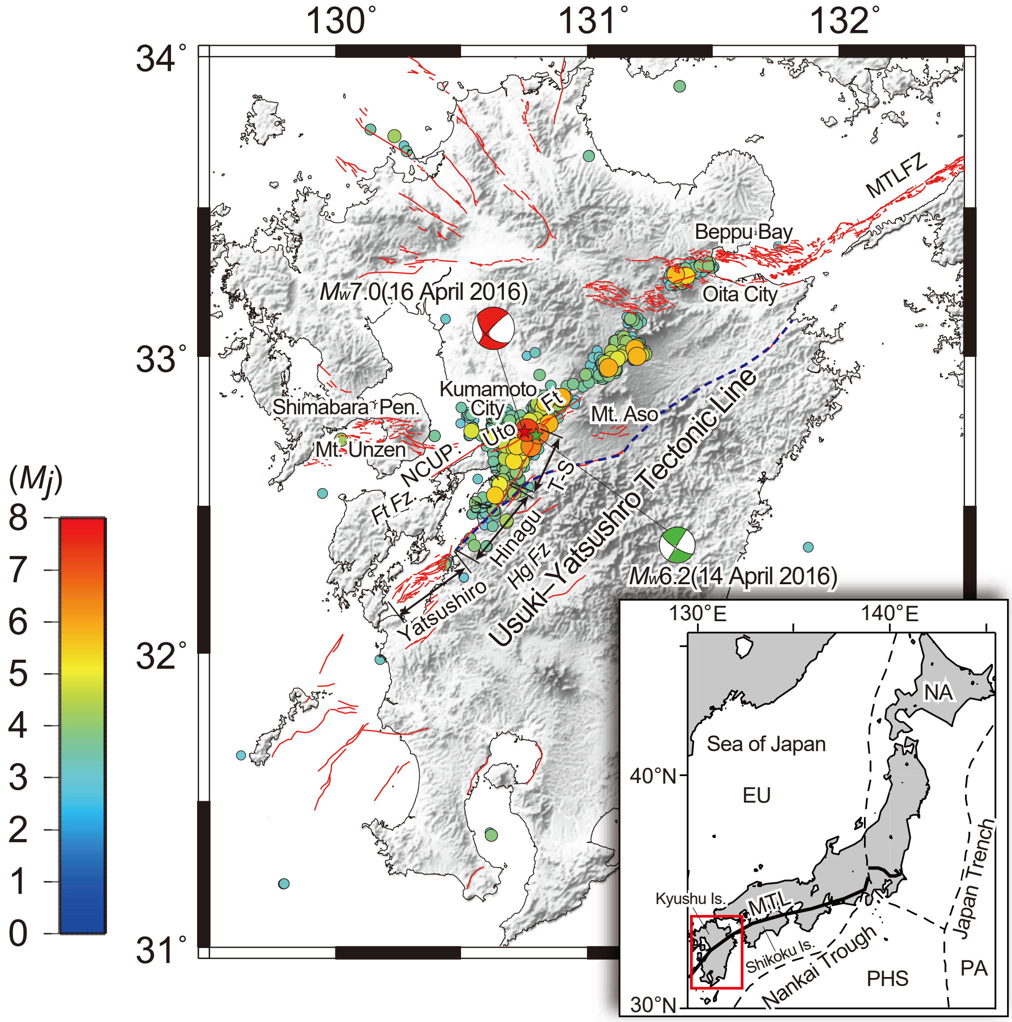

130°
131°
132°
34°
33°
32°
31°
(Mj)
8
7
6
5
4
3
2
1
0
MTLFZ
Beppu Bay
Oita City
Mw7.0(16 April 2016)
Kumamoto City
Shimabara Pen.
Mt. Unzen
Mt. Aso
Uto
Ft
NCUP
Ft Fz
T-S
Hinagu
Hg Fz
Yatsushiro
Usuki–Yatsushiro Tectonic Line
Mw6.2(14 April 2016)
130°E
140°E
40°N
30°N
Sea of Japan
EU
NA
Japan Trench
Kyushu Is.
MTL
Shikoku Is.
Nankai Trough
PHS
PA

**Figure 2.**

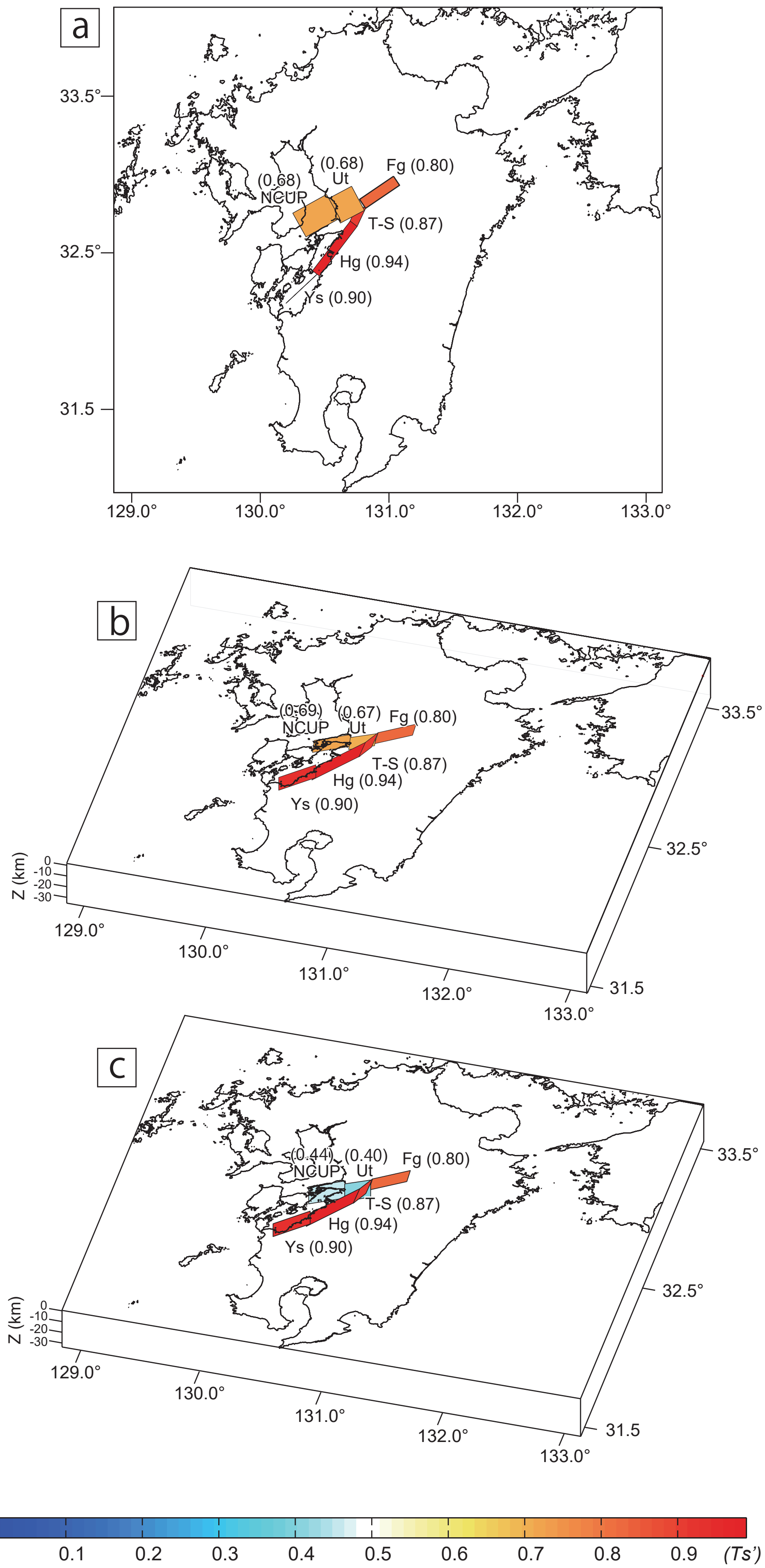

a
33.5°
32.5°
31.5
129.0°
130.0°
131.0°
132.0°
133.0°
(0.68)
NCUP
(0.68)
Ut
Fg (0.80)
T-S (0.87)
Hg (0.94)
Ys (0.90)
b
(0.69)
NCUP
(0.67)
Ut
Fg (0.80)
T-S (0.87)
Hg (0.94)
Ys (0.90)
Z (km)
0
-10
-20
-30
129.0°
130.0°
131.0°
132.0°
133.0°
33.5°
32.5°
31.5
c
(0.44)
NCUP
(0.40)
Ut
Fg (0.80)
T-S (0.87)
Hg (0.94)
Ys (0.90)
Z (km)
0
-10
-20
-30
129.0°
130.0°
131.0°
132.0°
133.0°
33.5°
32.5°
31.5
0
0.1
0.2
0.3
0.4
0.5
0.6
0.7
0.8
0.9
(Ts')

**Figure 3.**

(a)

Plane figure for a fault plane

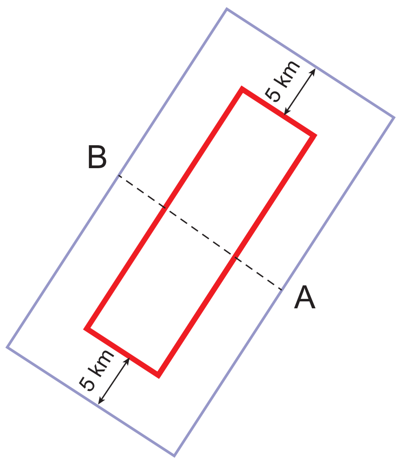


(b)

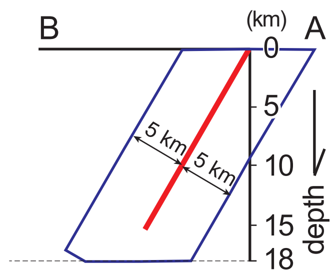


Cross section figure for a fault plane

**Figure 4.**

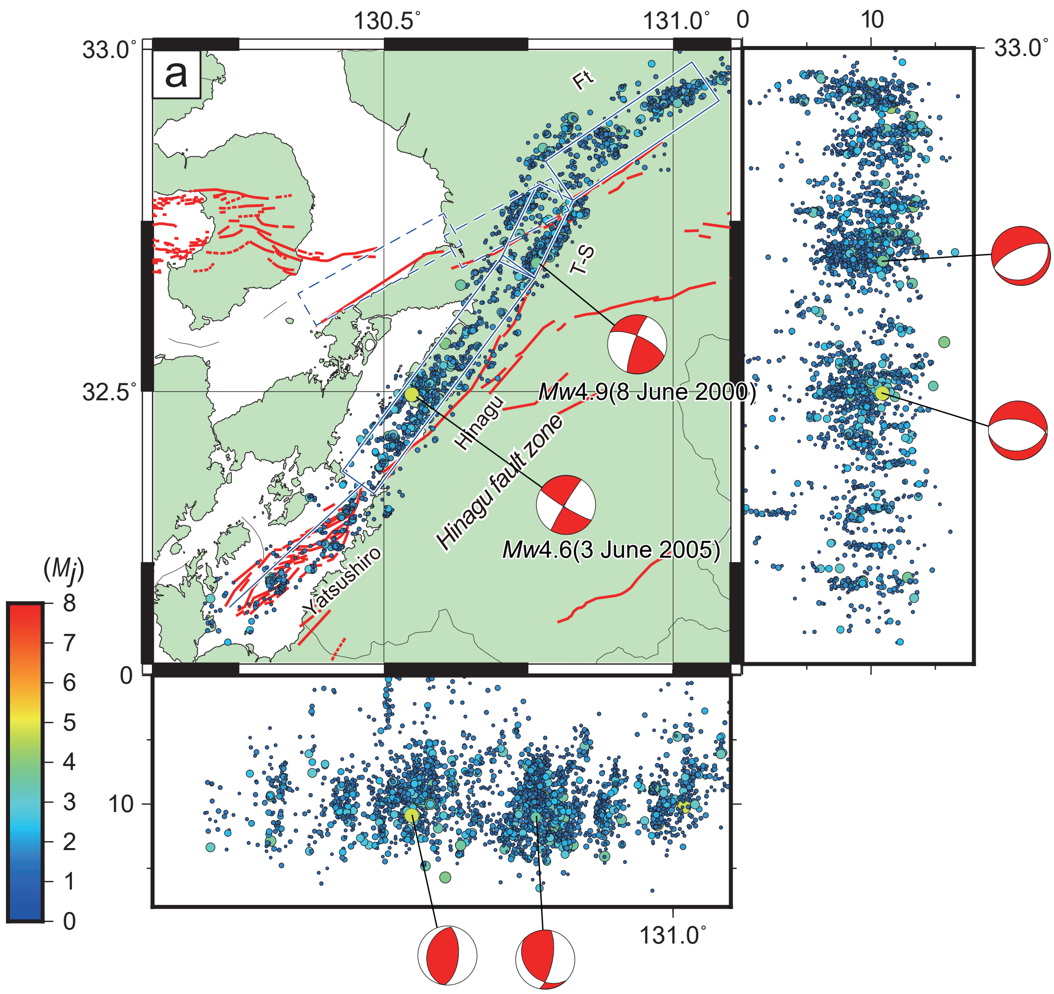
a
130.5°
131.0°
33.0°
32.5°
0
10
Ft
T-S
Hinagu
Hinagu fault zone
Yatsushiro
Mw4.9(8 June 2000)
Mw4.6(3 June 2005)
(Mj)
8
7
6
5
4
3
2
1
0

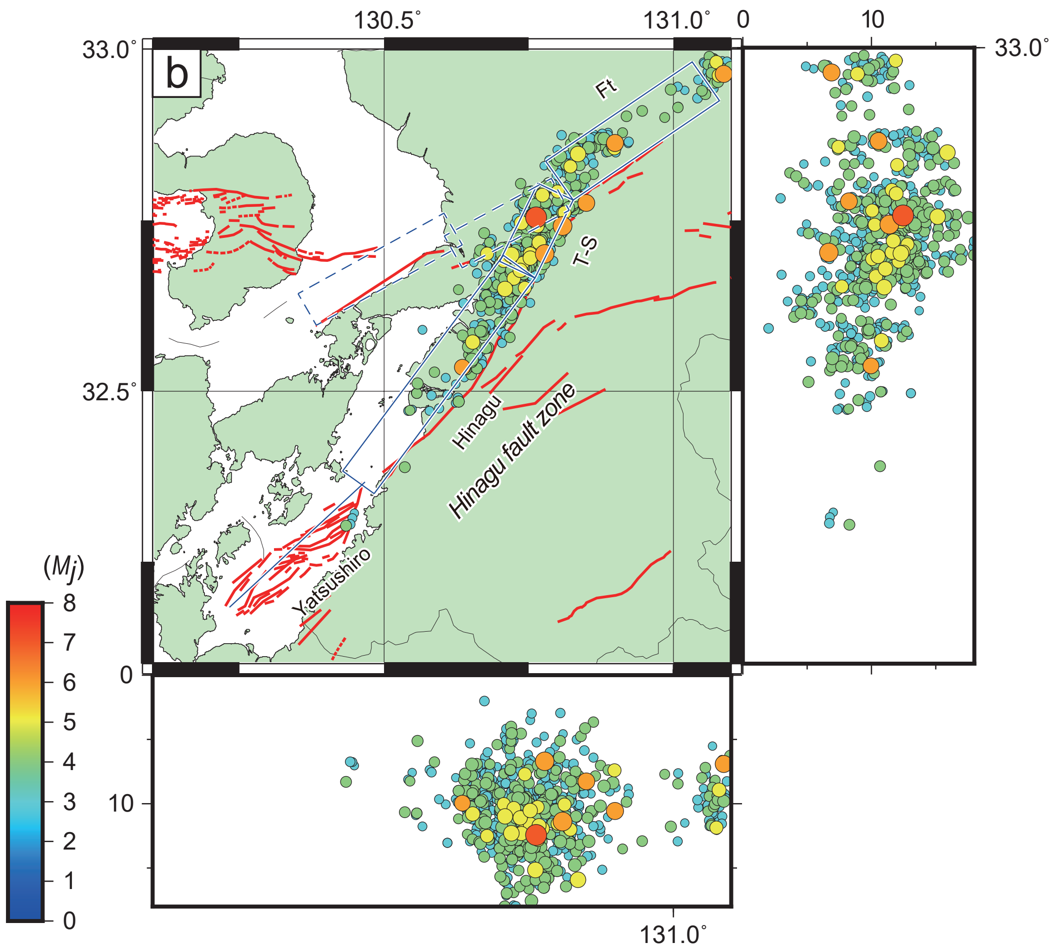
b
130.5°
131.0°
33.0°
32.5°
0
10
Ft
T-S
Hinagu
Hinagu fault zone
Yatsushiro
(Mj)
8
7
6
5
4
3
2
1
0

**Figure 5.**

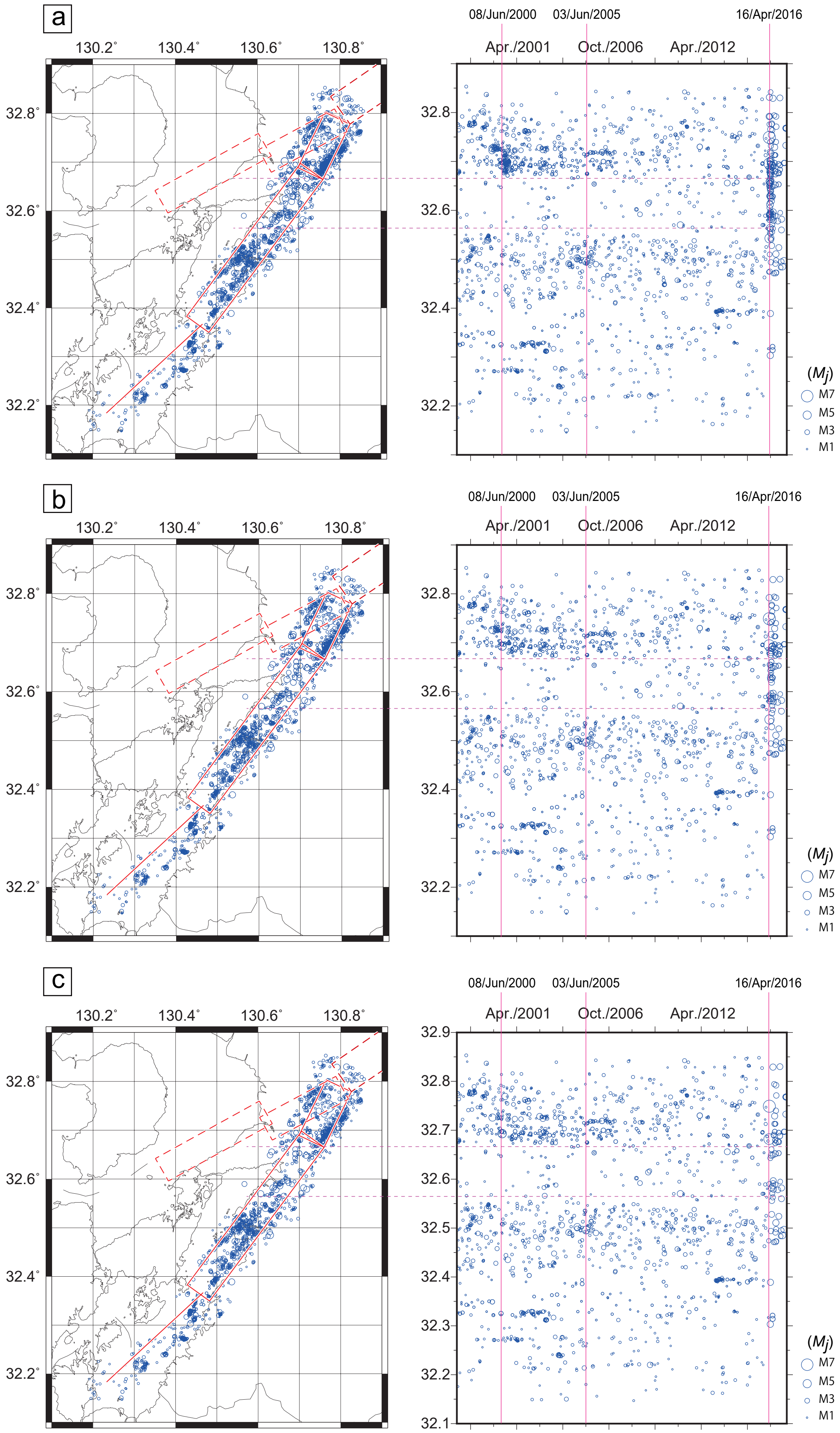

a
130.2°
130.4°
130.6°
130.8°
32.8°
32.6°
32.4°
32.2°
08/Jun/2000
03/Jun/2005
16/Apr/2016
Apr./2001
Oct./2006
Apr./2012
32.8
32.6
32.4
32.2
(Mj)
M7
M5
M3
M1
b
130.2°
130.4°
130.6°
130.8°
32.8°
32.6°
32.4°
32.2°
08/Jun/2000
03/Jun/2005
16/Apr/2016
Apr./2001
Oct./2006
Apr./2012
32.8
32.6
32.4
32.2
(Mj)
M7
M5
M3
M1
c
130.2°
130.4°
130.6°
130.8°
32.8°
32.6°
32.4°
32.2°
08/Jun/2000
03/Jun/2005
16/Apr/2016
Apr./2001
Oct./2006
Apr./2012
32.9
32.8
32.7
32.6
32.5
32.4
32.3
32.2
32.1
(Mj)
M7
M5
M3
M1

**Figure 6.**

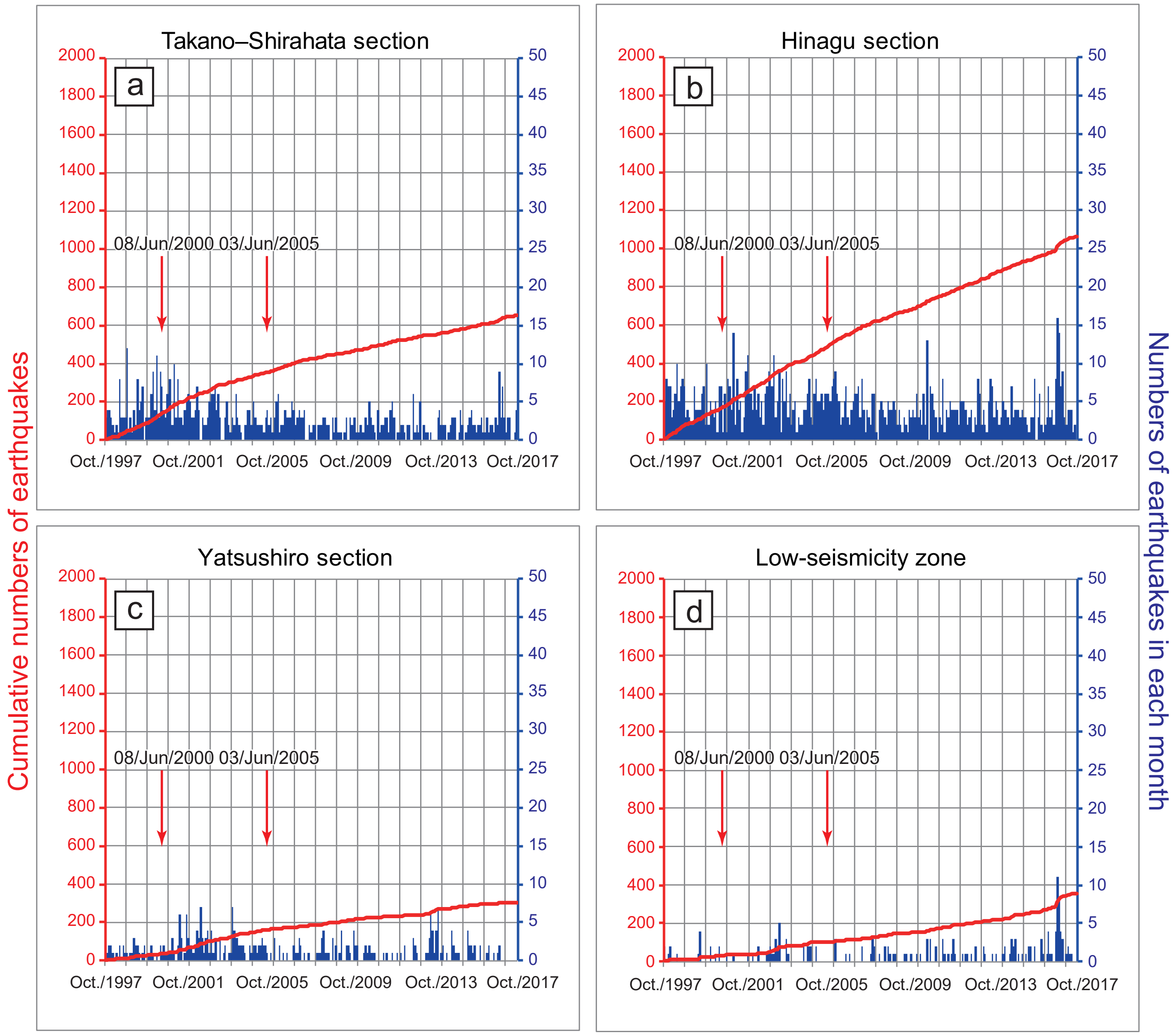

Takano–Shirahata section
a
Hinagu section
b
Yatsushiro section
c
Low-seismicity zone
d
08/Jun/2000
03/Jun/2005
2000
1800
1600
1400
1200
1000
800
600
400
200
0
50
45
40
35
30
25
20
15
10
5
0
Oct./1997
Oct./2001
Oct./2005
Oct./2009
Oct./2013
Oct./2017
Cumulative numbers of earthquakes
Numbers of earthquakes in each month

**Figure 7.**

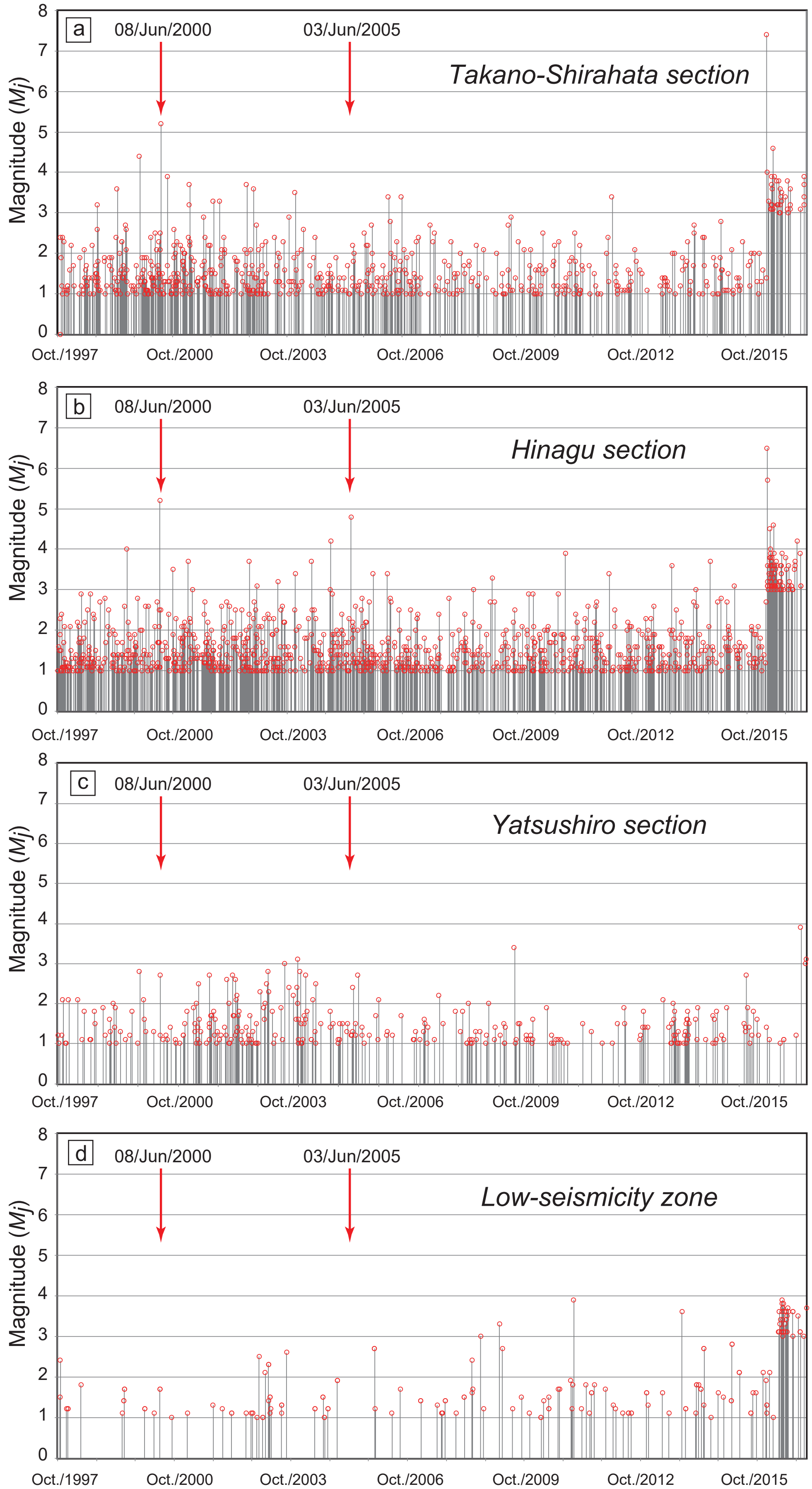

a
08/Jun/2000
03/Jun/2005
Takano-Shirahata section
b
08/Jun/2000
03/Jun/2005
Hinagu section
c
08/Jun/2000
03/Jun/2005
Yatsushiro section
d
08/Jun/2000
03/Jun/2005
Low-seismicity zone
Magnitude (Mj)
0
1
2
3
4
5
6
7
8
Oct./1997
Oct./2000
Oct./2003
Oct./2006
Oct./2009
Oct./2012
Oct./2015

**Figure 8.**

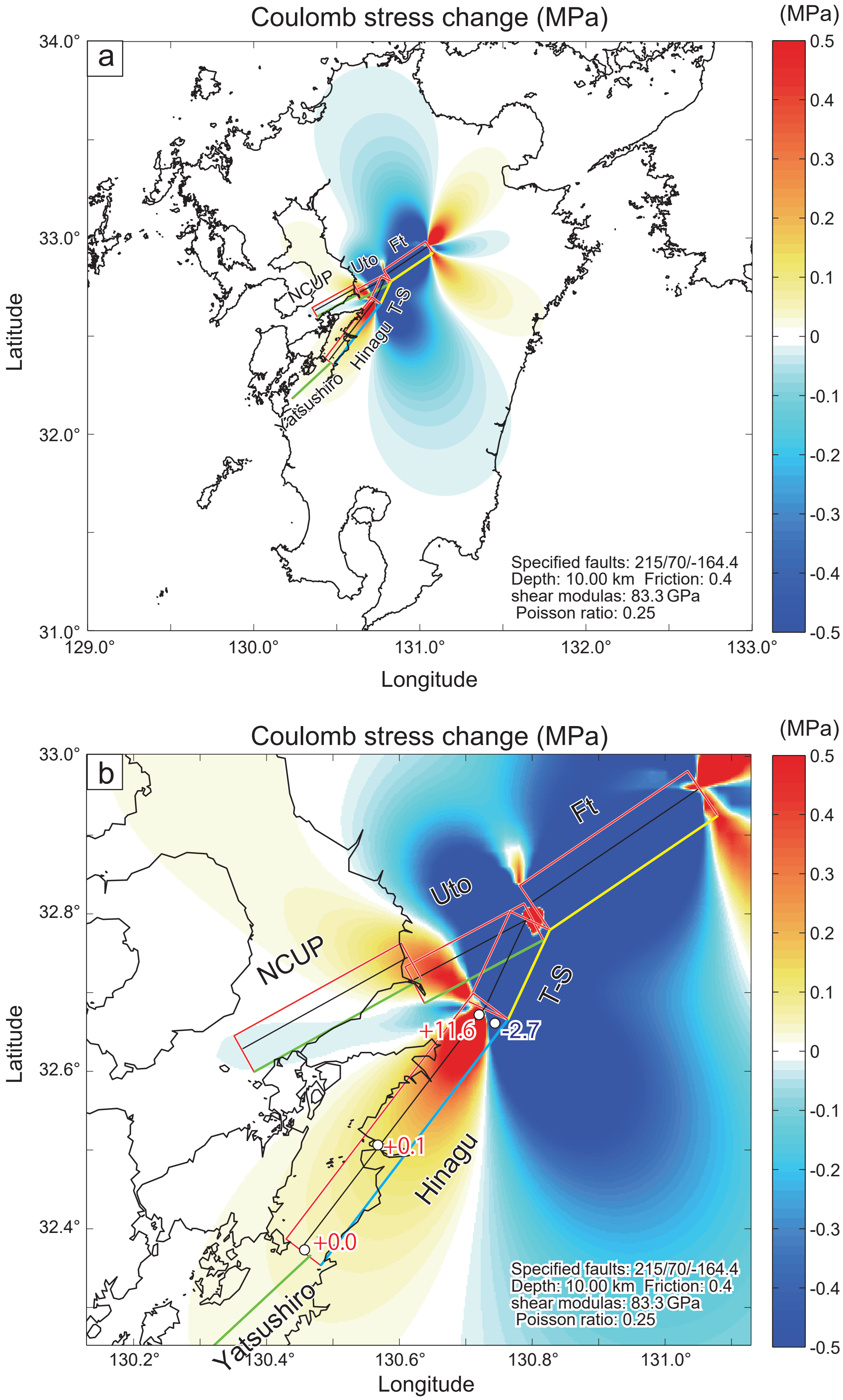

Coulomb stress change (MPa)
(MPa)
a
34.0°
33.0°
32.0°
31.0°
Latitude
129.0°
130.0°
131.0°
132.0°
133.0°
Longitude
NCUP
Uto
Ft
T-S
Hinagu
Yatsushiro
Specified faults: 215/70/-164.4
Depth: 10.00 km Friction: 0.4
shear modulas: 83.3 GPa
Poisson ratio: 0.25
0.5
0.4
0.3
0.2
0.1
0
-0.1
-0.2
-0.3
-0.4
-0.5
Coulomb stress change (MPa)
(MPa)
b
33.0°
32.8°
32.6°
32.4°
Latitude
130.2°
130.4°
130.6°
130.8°
131.0°
Longitude
Ft
Uto
NCUP
T-S
+11.6
-2.7
+0.1
+0.0
Hinagu
Yatsushiro
Specified faults: 215/70/-164.4
Depth: 10.00 km Friction: 0.4
shear modulas: 83.3 GPa
Poisson ratio: 0.25

**Figure 9.**

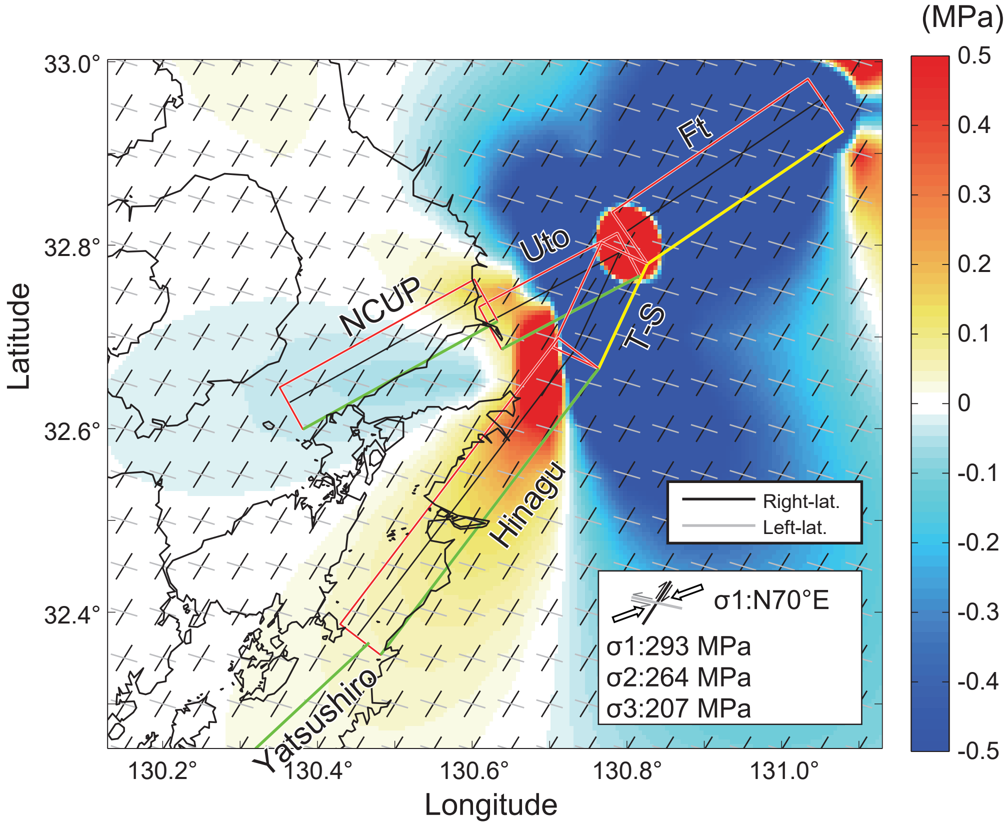

(MPa)
0.5
0.4
0.3
0.2
0.1
0
-0.1
-0.2
-0.3
-0.4
-0.5
33.0°
32.8°
32.6°
32.4°
Latitude
130.2°
130.4°
130.6°
130.8°
131.0°
Longitude
Ft
Uto
NCUP
T-S
Hinagu
Yatsushiro
Right-lat.
Left-lat.
σ1:N70°E
σ1:293 MPa
σ2:264 MPa
σ3:207 MPa

**Figure 10.**

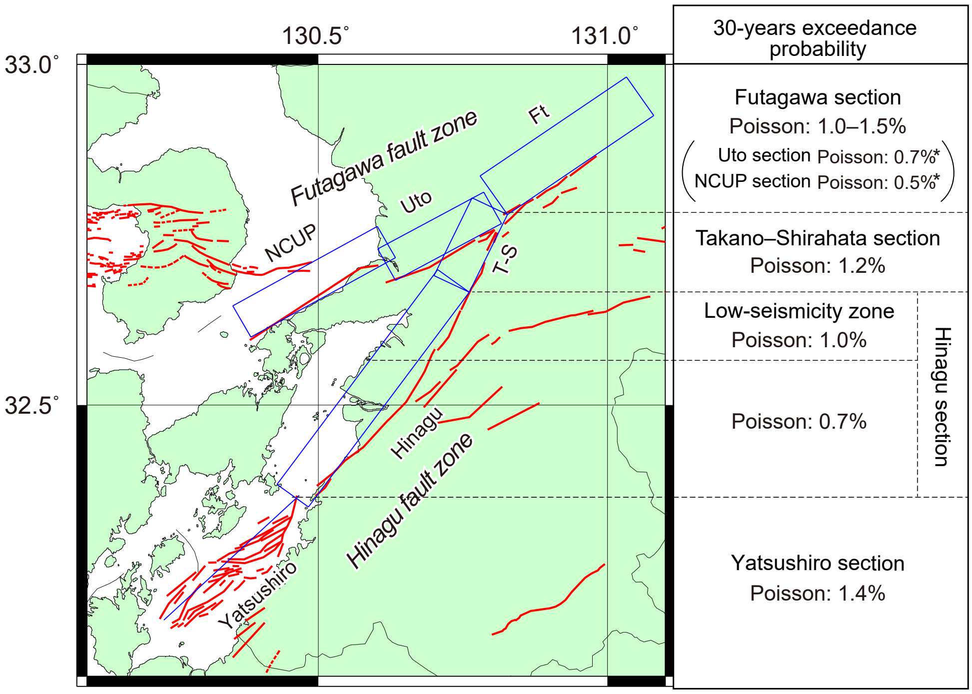
130.5°
131.0°
33.0°
32.5°
Futagawa fault zone
Ft
Uto
NCUP
T-S
Hinagu
Hinagu fault zone
Yatsushiro
30-years exceedance probability
Futagawa section
Poisson: 1.0–1.5%
Uto section Poisson: 0.7%*
NCUP section Poisson: 0.5%*
Takano–Shirahata section
Poisson: 1.2%
Low-seismicity zone
Poisson: 1.0%
Poisson: 0.7%
Hinagu section
Yatsushiro section
Poisson: 1.4%

**Figure 11.**

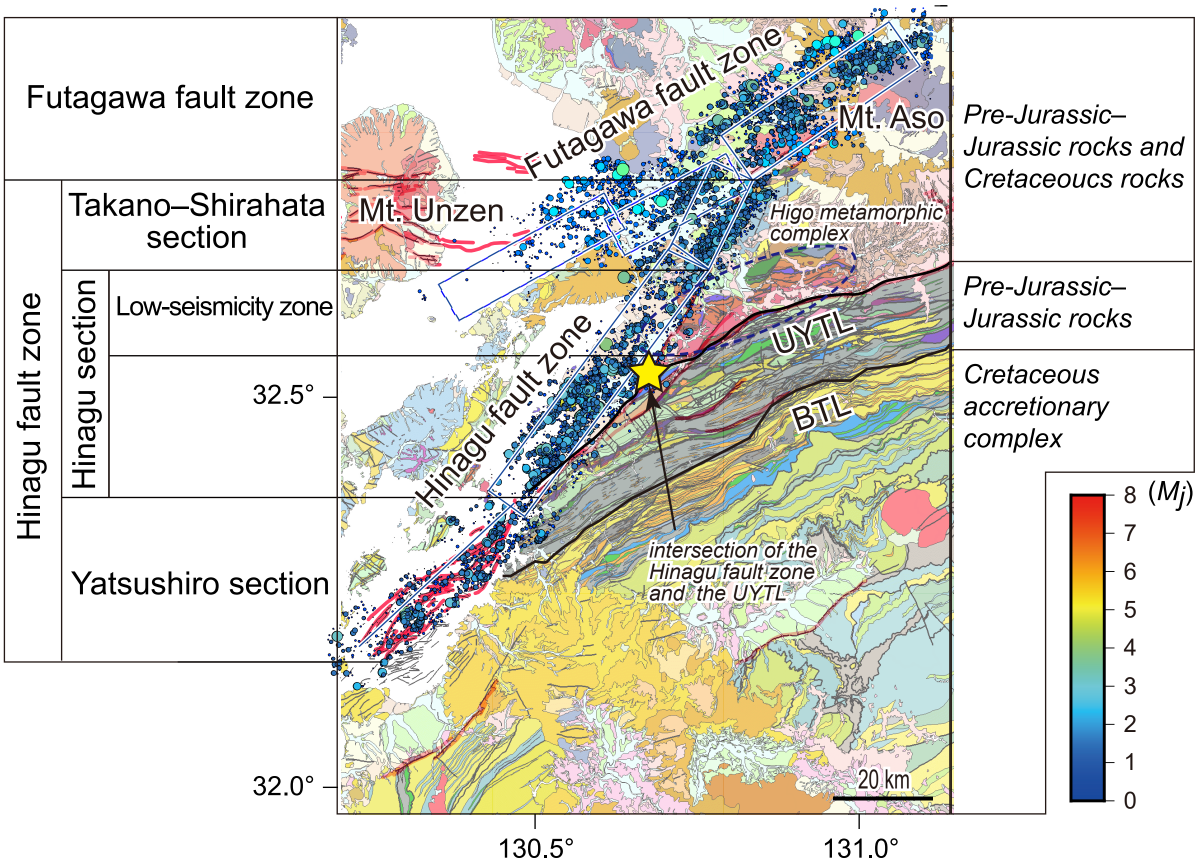

Futagawa fault zone
Hinagu fault zone
Takano–Shirahata section
Hinagu section
Low-seismicity zone
Yatsushiro section
Mt. Unzen
Mt. Aso
Higo metamorphic complex
UYTL
BTL
intersection of the Hinagu fault zone and the UYTL
Pre-Jurassic–Jurassic rocks and Cretaceoucs rocks
Pre-Jurassic–Jurassic rocks
Cretaceous accretionary complex
32.5°
32.0°
130.5°
131.0°
20 km
8 ($M_j$)
7
6
5
4
3
2
1
0